239

Self-similar compressible turbulent boundary layers with pressure gradients. Part 1. Direct numerical simulation and assessment of Morkovin's hypothesis

Christoph Wenzel[1,†]**, Tobias Gibis**[1]**, Markus Kloker**[1] **and Ulrich Rist**[1]

[1]Institute of Aerodynamics and Gas Dynamics, University of Stuttgart, 70550 Stuttgart, Germany

A direct numerical simulation study of self-similar compressible flat-plate turbulent boundary layers (TBLs) with pressure gradients (PGs) has been performed for inflow Mach numbers of 0.5 and 2.0. All cases are computed with smooth PGs for both favourable and adverse PG distributions (FPG, APG) and thus are akin to experiments using a reflected-wave set-up. The equilibrium character allows for a systematic comparison between sub- and supersonic cases, enabling the isolation of pure PG effects from Mach-number effects and thus an investigation of the validity of common compressibility transformations for compressible PG TBLs. It turned out that the kinematic Rotta–Clauser parameter β_K calculated using the incompressible form of the boundary-layer displacement thickness as length scale is the appropriate similarity parameter to compare both sub- and supersonic cases. Whereas the subsonic APG cases show trends known from incompressible flow, the interpretation of the supersonic PG cases is intricate. Both sub- and supersonic regions exist in the boundary layer, which counteract in their spatial evolution. The boundary-layer thickness δ_{99} and the skin-friction coefficient c_f, for instance, are therefore in a comparable range for all compressible APG cases. The evaluation of local non-dimensionalized total and turbulent shear stresses shows an almost identical behaviour for both sub- and supersonic cases characterized by similar β_K, which indicates the (approximate) validity of Morkovin's scaling/hypothesis also for compressible PG TBLs. Likewise, the local non-dimensionalized distributions of the mean-flow pressure and the pressure fluctuations are virtually invariant to the local Mach number for same β_K-cases. In the inner layer, the van Driest transformation collapses compressible mean-flow data of the streamwise velocity component well into their nearly incompressible counterparts with the same β_K. However, noticeable differences can be observed in the wake region of the velocity profiles, depending on the strength of the PG. For both sub- and supersonic cases the recovery factor was found to be significantly decreased by APGs and increased by FPGs, but also to remain virtually constant in regions of approximated equilibrium.

---

† Email address for correspondence: wenzel@iag.uni-stuttgart.de

1. Introduction

Most investigations of compressible turbulent boundary layers (TBLs) have been performed for zero streamwise pressure gradient (ZPG). In contrast to the ZPG TBL case, however, PG-influenced TBLs are difficult to study systematically since the pressure distribution can arbitrarily change in the streamwise direction, rendering the history of every spatially evolving PG TBL fairly unique (Vinuesa *et al.* 2017). The dynamic properties of the TBL are strongly influenced by this history even in the ZPG case (Perry, Marusic & Jones 2002) and thus strongly depend upon the specific distribution of the streamwise PG. In the incompressible regime, a fundamental part of understanding PG effects is therefore gained from self-similar PG TBLs, meaning that all or at least the most important terms of the governing equations have the same proportionality in their streamwise evolution. Since Reynolds-number effects are largely excluded and history effects clearly and reproducibly defined due to the equilibrium character of the resulting flow, PG effects can be isolated and generalized conclusions drawn, see Stratford (1959), Skåre & Krogstad (1994), Skote, Henningson & Henkes (1998), Lee & Sung (2008), Kitsios *et al.* (2016), Bobke *et al.* (2017), Kitsios *et al.* (2017) and Lee (2017).

In many aspects, the understanding of PG effects is more intricate in the compressible regime, even without taking the aspect of self-similarity into account. PGs are additionally linked for instance to Mach number and thus wall-temperature/ heat-flux variations in the streamwise direction. Supersonic boundary layers possess both a subsonic near-wall region and a supersonic outer part, and the overall effects of PGs are not readily predictable since the thickening of the boundary layer is the result of two opposing effects. While streamtubes tend to diverge for APGs in the subsonic near-wall region, they tend to converge in the supersonic outer part of the boundary layer (Smits & Dussauge 2006). Mainly caused by its spatially parabolic character and the presence of strong density variations in the wall-normal direction, the response of the supersonic PG TBL also highly depends on the way the PG is imposed. Different set-ups invoke additional phenomena strongly superimposing on the effect of 'pure' PGs. For compression ramps, for instance, the boundary layer is mainly affected by a (slightly oscillating) shock and a small region of separated flow in the corner, both significantly amplifying the level of turbulent fluctuations, see Ardonceau (1984), Dussauge & Gaviglio (1987), Smits & Muck (1987), Selig *et al.* (1989), Adams (2000), Wu & Martin (2007), Fang *et al.* (2015) and Sun, Hu & Sandham (2017), among others. Boundary layers over convex/concave curved surfaces, on the other hand, are additionally influenced by streamline curvature, wall-normal PGs, bulk dilatation and Görtler vortices, see Bradshaw (1973, 1974), Jayaram, Taylor & Smits (1987), Donovan, Spina & Smits (1994), Bowersox & Buter (1996), Arnette, Samimy & Elliott (1998), Luker *et al.* (2000), Tichenor, Humble & Bowersox (2013) and Wang, Wang & Zhao (2016*a*), for instance.

As a consequence, nearly everything known about pure PG effects on compressible TBLs has been gained from investigations of reflected-wave set-ups where the PG is imposed by a smoothly shaped body placed above a flat plate. The principal strain rate and the bulk dilatation are only slightly changed in the near-wall region along the streamwise direction in such flows (Wang, Wang & Zhao 2016*b*). Hence, the reflected-wave set-up is the only case which really allows the isolation and thus a meaningful discussion of pure PG effects in the compressible regime. Although the gross effects of PGs on compressible TBLs are understood or at least well described, a lot of fundamental questions remain.

One of the main problem seems to be that only a few experimental realizations (and no DNS data at all) of the reflected-wave set-up are available in the literature, and thus data being accurate or complete enough to verify theoretical results are lacking, see, e.g. Fernholz, Finley & Mikulla (1981), Fernholz *et al.* (1989), Fernando & Smits (1990), Smith & Smits (1997), Franko & Lele (2014), Wang *et al.* (2016*b*) and Wang, Wang & Zhao (2017). Compressibility transformations such as Morkovin's scaling or van Driest's transformation are derived under somewhat restrictive conditions which are assumed to be only approximately valid for the special case of the compressible ZPG TBL. Both, however, represent the basis for the description and thus our understanding of compressible TBLs, since they directly connect the compressible and incompressible regimes. This does not imply that they do not hold for PG cases, but due to the scarcity of data, their validity is not proven. In fact, experimental data transformed via van Driest's transformation show good agreement with incompressible data correlations for various wall-heating conditions and modest PGs. However, since the exact incompressible counterparts of the compressible problems are generally not known and often not even realizable for incompressible flows, this agreement is primarily qualitative (Cebeci & Bradshaw 1984). Furthermore, also the influence of PGs on the turbulent Prandtl number, the recovery factor and thus on the adiabatic wall temperature is unknown. All are of central importance for the derivation of turbulence models, as their success largely depends on the possibly physics-based modelling/universality of these values.

When considering the importance of compressible PG flows for e.g. commercial aviation or gas turbines, it would be highly desirable to extend the knowledge about pure PG effects on compressible TBLs by using DNS. These studies should be done with the same systematic approach as has been used for the incompressible regime so far by investigating self-similar PG TBLs. It is surprising, however, that virtually nothing is known from the analytical or numerical/experimental perspective about the canonical case of the compressible self-similar PG TBLs at all, despite the fact that its understanding/description should actually be the first step to understand PG effects in general in the compressible regime. It is not even clear to which degree any kind of self-similarity can be obtained in the turbulent compressible regime, if at all. It can certainly be expected that the compressible turbulent boundary-layer equations allow self-similar solutions due to the close relationship between the Favre-averaged and the incompressible Reynolds-averaged representations which are used as a starting point for self-similarity investigations. However, the concept of compressible self-similarity must compensate both Reynolds-number and compressibility effects caused by Mach-number variations in the streamwise direction, and its existence is not readily apparent.

1.1. *Objectives of this study*

It is the primary goal of this study to systematically investigate the effects of pure PGs on compressible TBLs by considering locally self-similar compressible PG TBLs via DNS. The equilibrium character of this canonical case should allow generalizable insight into the isolated effects of pure PGs on compressible turbulence and thus a well-described starting point for related investigations. Furthermore, it should allow for a direct comparison between compressible and incompressible cases (which are expected to be mutual counterparts) and thus the evaluation of compressibility transformations and Morkovin's hypothesis (Morkovin 1961), which have only been proven for ZPG TBLs so far.

The achievement of approximate self-similarity, however, cannot be assessed for flow data without understanding the theoretical conditions for self-similarity. Critical assumptions which have to be made for a compressible self-similarity analysis, however, cannot be verified without having data available. To this end, both a theoretically derived self-similarity analysis and results of carefully conducted DNS of self-similar compressible PG TBL are presented for the first time. Since only few investigations are available in the literature providing any detailed reference data of compressible PG TBLs, reliable DNS results are sought in general even without taking the aspect of self-similarity into account. The present investigations are therefore subdivided into two parts, the present first part which is mainly focused on the DNS results, and a second part which is mainly focused on the derivation/validation of compressible self-similarity, see Gibis *et al.* (2019).

The present study is structured as follows: in order to allow for a clear understanding of the present DNS study, both the numerical methodology and the numerical set-ups employed are summarized in §2. The following results section is split into two parts. While the first part (§3) mainly characterizes the spatial evolution of the resulting compressible flow fields, the validity of compressibility transformations applied to local mean-flow-field profiles is assessed in the second part (§4). Concluding remarks are given in §5.

2. Methodology and numerical set-up

First the modelling of the free-stream pressure distributions is presented, followed by a summary of the simulation parameters. To enable a clear interpretation of the results in the following, effects which are mainly caused by density variations due to a fixed non-small Mach number are referred to as compressibility effects. Shock-wave phenomena (by APGs), which may possibly occur, are referred to as supersonic effects. Quantities with an overbar represent quantities averaged in both the spanwise direction and time. The subscripts 'w' and 'e' refer to wall and free-stream quantities, respectively, see Wenzel *et al.* (2018*b*) for details.

2.1. *Methodology of the present study*

DNS results are computed for the canonical case of the self-similar (equilibrium) compressible PG TBL both for moderate APG and FPG cases. Therefore, all cases should be characterized by long distances of a constant kinematic Rotta–Clauser parameter $\beta_K = (\delta_K^*/\overline{\tau}_w)(\mathrm{d}p_e/\mathrm{d}x)$, where δ_K^* is the kinematic displacement thickness (see §3.2.1), $\overline{\tau}_w$ the mean wall shear stress and $\mathrm{d}p_e/\mathrm{d}x$ the pressure gradient in streamwise direction evaluated at the edge of the boundary layer. It was found that those regions still yield the state of approximate streamwise self-similarity in the compressible regime, see §4.1.1 and Gibis *et al.* (2019) for a detailed discussion. The use of both sub- and supersonic inflow Mach numbers should further allow for a meaningful comparison between the incompressible/subsonic and the compressible/supersonic regimes. As summarized in table 1, three nearly incompressible APG cases are investigated with inflow Mach numbers of $M_{\infty,0} = 0.5$, yielding Rotta–Clauser parameters of $\beta_K = 0.19$, 0.58 and 1.05. The subscript '∞' represents far-field values, the subscript '0' values evaluated at the inflow of the domain. For the compressible, supersonic regime four APG cases and one FPG case are investigated with inflow Mach numbers of $M_{\infty,0} = 2.0$, yielding $\beta_K = 0.15$, 0.42, 0.55 and 0.69 for the APG and $\beta_K = -0.18$ for the FPG case. Additionally, ZPG cases are computed for both inflow Mach numbers with the same set-up to provide

reference data for all PG cases. In order to benefit from the verified reliability of the ZPG set-ups, see Wenzel *et al.* (2018*b*), the same inflow Reynolds number of about $Re_\theta \approx 300$ is chosen for all cases.

2.2. *Numerical method*

All computations are performed with the compressible high-order in-house DNS code *NS3D*; fundamentals are described in Babucke (2009), Linn & Kloker (2008, 2011), Keller & Kloker (2014, 2016) and Wenzel *et al.* (2018*a*). With the velocity vector $\boldsymbol{u} = [u, v, w]^T$ with components in the streamwise, wall-normal and spanwise directions x, y and z, the dimensionless solution vector is $\boldsymbol{Q} = [\rho, \rho u, \rho v, \rho w, E]^T$, where ρ and E are the density and the total energy, respectively. Velocities and length scales are normalized by the streamwise reference velocity u_∞ and the reference length $L = \delta_{99,0}$, respectively, where $\delta_{99,0}$ is the boundary-layer thickness at the inflow of the domain. Temperature or density are normalized by the reference temperature T_∞ and the reference density ρ_∞; similarly for the thermal conductivity ϑ and the dynamic viscosity μ. Specific heats and the pressure p are non-dimensionalized by u_∞^2/T_∞ and $\rho_\infty u_\infty^2$, respectively. The ratio $\gamma = c_p/c_v = 1.4$ and the Prandtl number $Pr = 0.71$ are assumed constant. The temperature dependence of the viscosity is modelled by Sutherland's law and the linear law below the Sutherland temperature. The equations are solved on a block-structured Cartesian grid spanning a rectangular integration domain.

Either sixth-order subdomain-compact finite differences (FDs) or eighth-order explicit FDs are used for the three spatial directions, see Keller & Kloker (2013) or Babucke (2009), Keller (2016) and Dörr (2018), respectively; compact FDs are more stable for the supersonic cases. The classical explicit fourth-order Runge–Kutta scheme is used for time integration, coupled with alternating forward- and backward-biased FDs for the convective first derivatives, see Kloker (1997) and Babucke (2009).

2.3. *Numerical set-up and boundary conditions*

The numerical set-ups for the sub- and supersonic cases differ somewhat. For instance, the thickening of the boundary layer is less for supersonic than for subsonic APG cases, which effectively allows longer simulation domains for the same domain width in the supersonic case. Caused by the opposing effect of APGs on the effective grid resolution – increasing in the subsonic and decreasing in the supersonic case in terms of wall units for a fixed grid step – also the numerical grid has to be designed independently for both regimes. Furthermore, the pressure distribution noticeably varies across the far field – initially it is determined for the edge of the boundary layer but prescribed at the upper boundary of the simulation domain. The height of the domain thus has to be restricted to a minimum to minimize the distortion of the pressure distribution reaching the boundary layer. The set-ups for the sub- and supersonic cases are described below independently.

2.3.1. *Subsonic cases*

A sketch of the subsonic simulation domain is presented in figure 1. The main region of the computational box (red framed in figure 1*a,b*) is designed with a height of at least three boundary-layer thicknesses $\delta_{99,end}$ in the wall-normal y-direction, measured at the end of the main region x_{end} for the most restricting $\beta_K = 1.05$ case. The width is approximately $\pi \delta_{99,end}$ in the spanwise z-direction. Measured in boundary-layer thicknesses at the inflow of the simulation domain
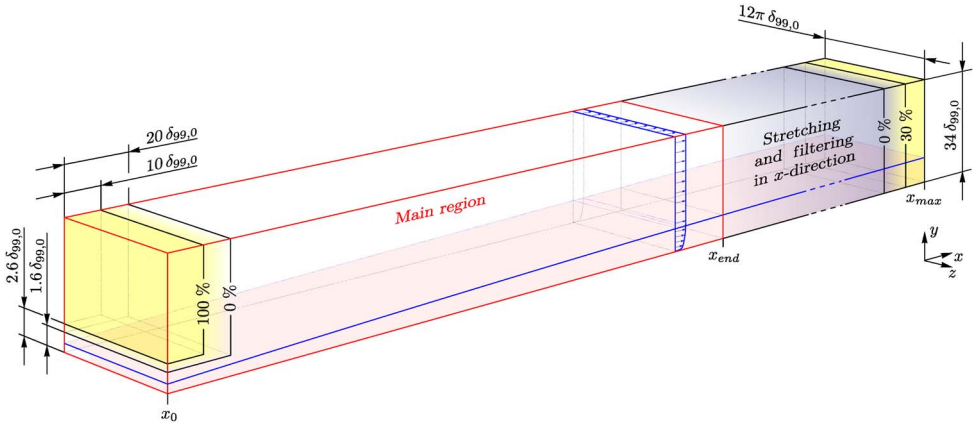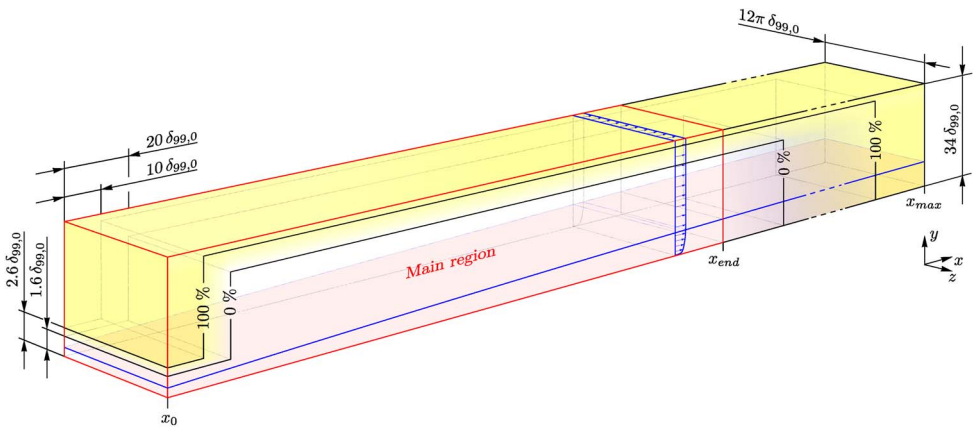
FIGURE 1. (Colour online) Simulation domain for present subsonic PG simulations. The yellow coloured regions represent sponge zones, blue shaded regions between x_{end} and x_{max} regions where grid stretching is applied in the streamwise direction to make spatial filtering effective. The red-bordered zone represents the main region of the simulations. (*a*) Simplified simulation domain for the calculation of physical mean values for sponge-zone application. (*b*) Simulation domain for the final calculation. The yellow coloured sponge regions force the unsteady flow to the previously calculated mean-flow values, which are set as new base-flow values.

($Re_\theta \approx 300$), the main region of the computational box has a dimension of $340\,\delta_{99,0} \times 34\,\delta_{99,0} \times 12\pi\,\delta_{99,0}$, respectively. The length of the PG set-up in the streamwise x-direction thus corresponds to 73 % of the ZPG case discussed in Wenzel *et al.* (2018*b*) whereas the width corresponds to 150 %.

At the solid wall, the flow field is treated as fully adiabatic at every time instance with $(dT/dy)_w = 0$, which suppresses any heat exchange between the wall and fluid; the pressure at the wall is calculated by $(dp/dy)_w = 0$. For the velocity components, the no-slip impermeable wall BC is applied. At the outflow, the time derivative, respectively the complete space operator, is extrapolated with $\partial \mathbf{Q}/\partial t|_N = \partial \mathbf{Q}/\partial t|_{N-1}$ corresponding to a first-order extrapolation. At the top of the domain, p, T and thus also ρ are kept constant. The velocity components u and w are specified by $d/dy = 0$; the wall-normal velocity component v is calculated from the continuity equation

under the assumption of $\mathrm{d}\rho/\mathrm{d}y = 0$ such that $\mathrm{d}v/\mathrm{d}y = -1/\rho(\mathrm{d}(\rho u)/\mathrm{d}x + \mathrm{d}(\rho w)/\mathrm{d}z)$. Caused by the non-characteristic behaviour of this BC, the additional application of numerical grid stretching and filtering and/or additional sponge zones is necessary if sound-wave reflection should be suppressed. At the inflow, a digital-filtering synthetic-eddy-method (SEM) approach is used to generate an unsteady, turbulent inflow condition, see Wenzel *et al.* (2018*b*) or Wenzel (2019). The spanwise direction is treated as periodic.

In order to allow a smooth transition process with a defined state from the pseudo-physical to a fully developed turbulent state, a ZPG region with a spatial extent of $30\delta_{99,0}$ is applied at the inflow of the domain before the PG is forced, see § 2.4. The induction distance for reaching fully developed turbulence is therefore the same as for the ZPG case at $M_\infty = 0.5$ ($\Delta x_{ind}/\delta_{99,0} \approx 28$, see table 2 and Wenzel *et al.* (2018*b*)), and similar for all PG distributions. A sponge region is applied outside the boundary layer at the inflow to prevent the included far-field flow from being unduly distorted by the transient process, see Schmidt (2014), Kurz & Kloker (2014) and Wenzel (2019). The sponge zone fixes the constant pressure region in the far field through the inflow region, which otherwise is strongly influenced by the retroactive effect of the PG applied further downstream. Only in the streamwise direction, geometrical grid stretching is applied to the numerical grid in the outflow region, see Wenzel (2019).

Due to the limited height of the simulation domain, the realizable total grid cell increase and thus the effect of the numerical filter is limited in the wall-normal direction in the far field of the domain. Possible reflections occurring at the far-field boundary are therefore suppressed by the application of additional sponge zones. These are to damp the unsteady flow to a prescribed mean flow not known *a priori*. To generate this mean flow, a precursor simulation is computed on a preliminary set-up for all PG cases, see figure 1(*a*). Weak reflections occurring at the far-field boundary are not treated by this set-up since they have been found to average out in the temporal mean. The accuracy of the resulting flow field has been verified by a comparison with the ZPG case given in Wenzel *et al.* (2018*b*). At the outlet of the simulation domain, a small sponge zone is applied to avoid a temporal drift of the outlet pressure. This sponge damps the flow field to a spatially undeveloped reference solution defined *a priori*. Hence, to minimize the distortion of the flow field, its effectiveness is reduced to 30 % of the inflow sponge. The resulting mean flow is used as a new base flow for the final set-up in a second step, which allows the application of additional sponge zones at the far-field boundary and the outflow region, both with the same effectiveness as the inflow sponge. A sketch of the final set-up is given in figure 1(*b*).

2.3.2. *Supersonic cases*

A sketch of the supersonic simulation domain is depicted in figure 2. Caused by the spatially hyperbolic behaviour of the supersonic flow, the pressure information is only allowed to move along the angle of the flow's local characteristics. Thus, prescribed by the far-field BC at the top of the domain, the information of the particular PG is diagonally transmitted as Mach waves (shock waves if the PG is too strong) down to the plate (black solid lines in figure 2) where they are reflected (black dashed lines). The final pressure field results from the superposition of the prescribed, incoming and the reflected, outgoing waves. Both yield a complex flow field with lines of constant pressure being almost perpendicular to the wall for regions of fully established wave systems (cyan coloured solid lines). The induction length (inflow region in figure 2) therefore depends on the Mach number, the length of the ZPG inflow region and the height of the simulation domain. Hence, it is fixed by the particular numerical set-up.
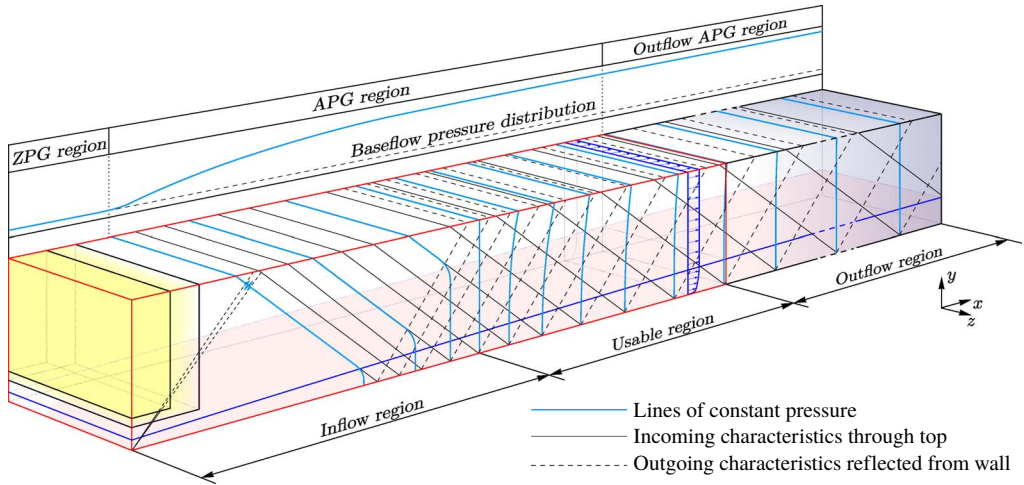
FIGURE 2. (Colour online) Simulation domain for present supersonic PG simulations. The yellow and blue shaded regions represent sponged and grid-stretched zones, respectively. The main region of the simulation is red bordered. Pressure information introduced at the far field moves diagonally to the wall (black solid lines) and is reflected (black dashed lines). The final pressure field is depicted by cyan coloured solid lines.

For the present simulations, the main region of the computational box (red framed in figure 2) is designed with a height of at least three boundary-layer thicknesses $\delta_{99,end}$ in the wall-normal y-direction and a width of approximately $\pi\,\delta_{99,end}$ in the spanwise z-direction for the most restricting $\beta_K = 0.69$ case. Measured in boundary-layer thicknesses at the inflow of the simulation domain ($Re_\theta \approx 300$), the main region of the computational box has a dimension of $500\,\delta_{99,0} \times 34\,\delta_{99,0} \times 12\pi\,\delta_{99,0}$, respectively. The length of the PG set-up in the streamwise x-direction thus corresponds to 107 % of the ZPG cases discussed in Wenzel *et al.* (2018*b*) and 147 % of the previously presented subsonic PG cases.

The outflow is parabolized by neglecting the second x-derivatives; biased difference stencils are used for the first x-derivatives. At the top of the simulation domain, a subsonic characteristic outflow BC is applied according to Poinsot & Lele (1991) (see also Babucke (2009), Franko & Lele (2014)). Its implementation allows upward travelling (outgoing) disturbances to leave the integration domain, whereas downward travelling (incoming) disturbances are set to zero in order to avoid reflections. This BC, in fact, allows the mean pressure to adapt at the upper boundary, see below. A detailed justification and discussion of its use is given in Wenzel (2019).

Following the same ideas as for the subsonic set-ups, a ZPG region with a spatial extent of $80\,\delta_{99,0}$ is applied at the inflow of the domain before the PG is forced (see next section for details). The induction distance until turbulence is fully developed is therefore the same as for the ZPG case at $M_\infty = 2.0$ ($\Delta x_{ind}/\delta_{99,0} \approx 60$, see table 2 and Wenzel *et al.* (2018*b*)), and identical for all different PG distributions. As for the subsonic cases, an identically dimensioned sponge region is applied at the inflow of the domain to absorb the shock system which is caused by the transient process of the inflow BC. It is noted that the prescribed wall-normal velocity component v, to which the flow field is damped down in the sponge region, has to closely match the one generated by the boundary layer itself. A mismatch of both velocities causes a

discontinuity (exemplarily given in figure 2 as dotted lines at the inflow), which is reflected by the upper boundary and thus affects the flow field in the whole simulation domain. A detailed derivation of an analytical velocity adaption procedure can be found in Gibis (2018). The outflow region of the simulation domain is only slightly stretched and filtered to avoid reflections from the outflow BC in the subsonic near-wall regions of the boundary layer. It was found that no additional outflow sponge region is required.

2.4. *Modelling of the free-stream pressure distribution*

In the incompressible regime, the self-similar state of the PG TBL is usually predicted by evaluation of the non-dimensional Rotta–Clauser parameter $\beta_K = (\delta_K^*/\overline{\tau}_w)\,(\mathrm{d}p_e/\mathrm{d}x)$, which must be constant for all streamwise positions. Following the idea of Townsend (1956), this state is achieved if the streamwise velocity at the edge of the boundary layer u_e follows the power-law relation $u_{PG}(x) = \alpha(x - x_{origin})^m$, with the PG strength exponent m, a scaling parameter $\alpha = u_{PG}(x_{PG,start})$ and the virtual origin of the boundary layer x_{origin}. Based on the analytical investigations and the assumptions made therein, both definitions are assumed to approximately still hold for the compressible regime, see Gibis *et al.* (2019).

The corresponding temperature and pressure distributions are calculated from the one-dimensional isentropic gas equations

$$T_{PG}(x) = T_t - \frac{\dfrac{\gamma - 1}{2}u_{PG}(x)^2}{\gamma R}, \quad p_{PG}(x) = \frac{p_t}{\left(1 + \dfrac{\gamma - 1}{2}M_{PG}(x)^2\right)^{\gamma/(\gamma-1)}}, \qquad (2.1a,b)$$

with the Mach number $M_{PG}^2 = u_{PG}^2/(\gamma R T_{PG})$, the total temperature T_t and total pressure p_t calculated at the inflow of the simulation domain as well as the isentropic exponent γ. The distribution of the far-field density is calculated from the equation of state $\rho_{PG} = p_{PG}/(R T_{PG})$. The particular values describing the respective velocity and thus the pressure distributions are summarized in table 1. Note that the definition of the pressure distribution at the top of the simulation domain yielding a requested β_K-value is the result of an iterative procedure, since both the correlation between m and β_K as well as the exact value of x_{origin} are unknown *a priori*.

Figure 3 visualizes both the initially implied (p_{PG}, u_{PG}) and the resulting pressure and velocity distributions after being adapted by the particular BC (p_{top}, u_{top}, v_{top}), all evaluated at the top of the simulation domains. The subsonic pressure distributions are fixed by the subsonic free-stream BC to the prescribed values $p_{PG} = p_{top}$ in figure 3(*a*) and thus also approximately the streamwise velocity component $u_{PG} \approx u_{top}$ in figure 3(*b*). The supersonic initial distributions are adapted by the free-stream BC in such a way that the pressure at the far-field boundary matches the pressure of the resulting flow field inside the domain, see Franko & Lele (2014) and Wenzel (2019). The resulting pressure distributions still follow an approximated power-law relation (blue/cyan for the prescribed distributions p_{PG}, grey for the resulting distributions p_{top}, only given for the $cAPG_{\beta_K=0.69}$ and $cFPG_{\beta_K=-0.18}$ case). The resulting distributions for the streamwise velocity component u_{top} are given in

				Start PG $[x/\delta_{99,0}]$	x_{origin} $[x/\delta_{99,0}]$	m $[-]$	Smooth $[x/\delta_{99,0}]$	β_K $[-]$	β $[-]$
(1)	——	(red)	iZPG	—	—	—	—	0.00	0.00
(2)	—— · ·	(red)	iAPG$_{\beta_K=0.19}$	30	−33.3	−0.07	—	0.19	0.21
(3)	— · —	(red)	iAPG$_{\beta_K=0.58}$	30	−33.3	−0.15	—	0.58	0.62
(4)	··········	(red)	iAPG$_{\beta_K=1.05}$	30	−33.3	−0.20	—	1.05	1.08
(5)	——	(blue)	cZPG	—	—	—	—	0.00	0.00
(6)	—— –	(blue)	cAPG$_{\beta_K=0.15}$	80	−183.3	−0.08	10–135	0.15	0.24
(7)	— —·	(blue)	cAPG$_{\beta_K=0.42}$	80	−183.3	−0.20	10–135	0.42	0.64
(8)	— — —	(blue)	cAPG$_{\beta_K=0.55}$	80	−183.3	−0.25	10–135	0.55	0.82
(9)	············	(blue)	cAPG$_{\beta_K=0.69}$	80	−183.3	−0.29	10–135	0.69	1.00
(10)	—— · · ·	(cyan)	cFPG$_{\beta_K=-0.18}$	80	−183.3	0.10	10–135	−0.18	−0.34

TABLE 1. Initial values for the PG cases. Given parameters are the starting point of the PG region in boundary-layer thicknesses at the inflow of the domain $\delta_{99,0}$, the virtual origin of the velocity distribution x_{origin}, the PG strength exponent m, smoothed regions between ZPG and PG regions and the resulting β_K and β parameters, if computed with the incompressible and compressible displacement thicknesses δ_K^* and δ^*, respectively.

figure 3(*b*) and show reciprocal trends. The wall-normal velocity component v_{top} is given in figure 3(*c*). Whereas subsonic APG and supersonic FPG cases correspond to diverging nozzle flows with positive v-components, supersonic APG and subsonic FPG cases correspond to converging nozzle flows with negative v-components. It is noted that the strongest APG case decelerates the far-field flow by approximately 35 %, resulting in a maximum wall-normal velocity component v_{top} of approximately 8 % of the streamwise velocity component u_{top}.

2.5. *Simulation parameters*

The grid resolution for all subsonic cases is based on the most restricting one which is the *iZPG* case (*i* for quasi incompressible), which thus allows the application of the same resolution criteria as for the ZPG study evaluated in Wenzel *et al.* (2018*b*). For all supersonic cases, the grid resolution is based on the most restricting $cAPG_{\beta_K=0.69}$ case. Its grid resolution is comparable to the ZPG $M_\infty = 2.0$ case given in Wenzel *et al.* (2018*b*). A grid convergence analysis for the two most restricting cases is given in appendix A. The numerical grid for the sub- and supersonic cases consists of $2500 \times 270 \times 820$ and $5000 \times 300 \times 960$ grid points in the three dimensions, respectively, both with additional 200 points appended in the outflow region in the streamwise direction. Whereas each subsonic set-up consists of 597 780 000 total grid points, each supersonic set-up consists of 1 497 600 000 total grid points. The resulting grid resolution in wall units is summarized in table 3(b) for all cases; it is evaluated for the usable region where almost constant β_K-values can be found, see figure 10. Table 3(a) summarizes additional information characterizing the spatial extent of the numerical simulation domain for all cases. The reference thermodynamic flow properties are the inflow far-field temperature $T_\infty = 288.15$ K, inflow far-field density $\rho_{PG,\infty} = 1.225$ kg m^{-3}, Prandtl number $Pr = 0.71$, specific gas constant $R = 287$ J kg^{-1} K^{-1} and ratio of specific heats $\gamma = 1.4$ and are set equal for all cases.
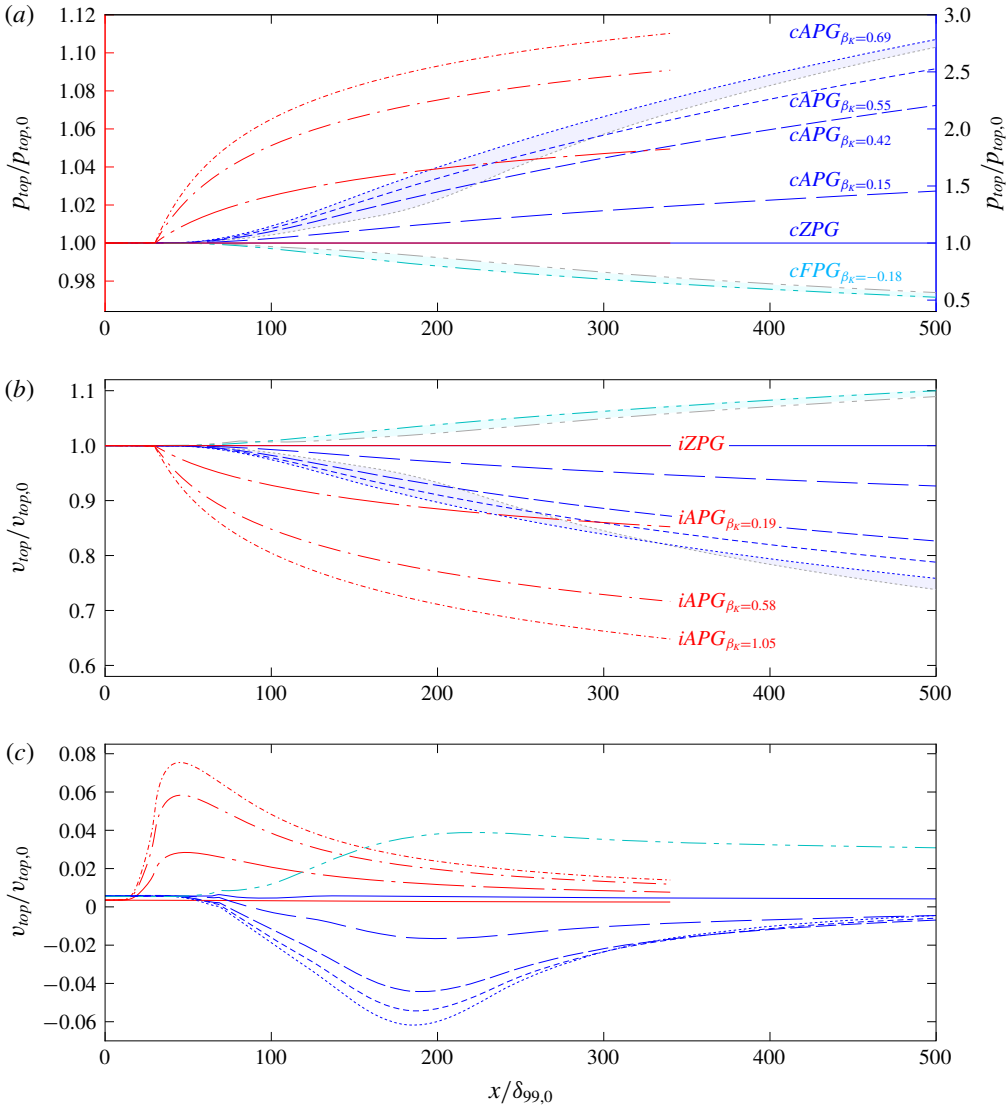
FIGURE 3. (Colour online) (*a*) Pressure p for subsonic cases (left axis) and supersonic cases (right axis), and (*b,c*) u- and v-velocity components. All distributions are evaluated at the top of the simulation domain (index '*top*'). Red lines correspond to subsonic, blue and cyan lines to supersonic cases. Whereas the subsonic far-field BC fixes the pressure distribution $p_{top} = p_{PG}$, the supersonic BC allows the pressure to adapt. The initially prescribed values (index '*PG*') are represented as coloured lines, the adapted states (index '*top*') as grey lines only given for $cAPG_{\beta_K=0.69}$ and $cFPG_{\beta_K=-0.18}$.

Data averaging is performed over both time and spanwise direction and does not start before the flow has passed the whole simulation domain at least twice. An overview of the time-averaging periods Δt used for all cases is given in table 2. Consistently for all cases, time averages were performed over a flow-through time corresponding to approximately 250 local boundary-layer thicknesses δ_{99}, see $\Delta t u_e/\delta_{99}$ in table 2.

		$\Delta t u_e/\delta^*$	$\Delta t u_e/\delta_{99}$	$\Delta t u_\tau^2/\overline{\nu}_w$	FTT	$\Delta x_{ind}/\delta_{99,0}$
(1)	iZPG	3373–1540	621–282	10 841–8720	5.3	28
(2)	$iAPG_{\beta_K=0.19}$	3375–1510	674–296	11 008–7824	6.6	28
(3)	$iAPG_{\beta_K=0.58}$	2463–1152	554–250	8457–5540	7.0	28
(4)	$iAPG_{\beta_K=1.05}$	2527–1248	617–300	8956–5716	9.6	28
(5)	cZPG	2379–984	712–295	8867–6874	5.4	60
(6)	$cAPG_{\beta_K=0.15}$	2208–207	665–346	9753–8734	6.2	60
(7)	$cAPG_{\beta_K=0.42}$	1777–967	544–266	7994–7246	5.0	60
(8)	$cAPG_{\beta_K=0.55}$	2454–1294	751–353	11 057–9650	6.8	60
(9)	$cAPG_{\beta_K=0.69}$	1927–987	594–271	8760–7419	5.4	60
(10)	$cFPG_{\beta_K=-0.18}$	1394–639	412–204	5989–4123	4.0	60

TABLE 2. Summary of time-averaging parameters measured at the begin and end of the usable region, see figure 10. $\Delta t u_e/\delta^*$ and $\Delta t u_e/\delta_{99}$ give the number of local boundary-layer thicknesses δ_{99} and local displacement thicknesses δ^*, which have been streamed through during Δt. $\Delta t u_{\tau,0}^2/\nu_w$ represents Δt in wall units Δt^+. The number of flow-through times (FTT) gives the number of time-averaged runs through the main region. $\Delta x_{ind.}/\delta_{99,0}$ gives the induction distance needed to reach a fully turbulent state, see Wenzel *et al.* (2018*b*).

3. Results for the untransformed, compressible flow fields

No DNS data are available in the literature for the reflected-wave set-up. It is the primary goal of this section to characterize the resulting flow-field data first by evaluating the spatial evolution of essential boundary-layer quantities. Additionally, some characteristic features of the instantaneous turbulent flow fields are shortly presented; their detailed interpretation will be part of future studies. The most common compressibility transformations are evaluated and discussed in § 4.

3.1. *Two- and three-dimensional flow fields*

Figures 4 and 5 show the mean-pressure field $\overline{p}/p_{\infty,0}$ and the wall-normal velocity component $\overline{v}/u_{\infty,0}$ of (*a*) the strongest subsonic $iAPG_{\beta_K=1.05}$ case, (*b*) the strongest supersonic $cAPG_{\beta_K=0.69}$ case and (*c*) the supersonic $cFPG_{\beta_K=-0.18}$ case; the outflow region is cropped. The boundary-layer thickness δ_{99} is depicted by black dash-dotted lines.

A fully developed pressure field – characterized by lines of constant pressure along *y* outside the boundary layer (black solid lines) – is achieved for the subsonic $iAPG_{\beta_K=1.05}$ case for $x/\delta_{99,0} \gtrsim 50$ (figure 4*a*). For the supersonic cases, this induction distance is elongated up to $x/\delta_{99,0} \gtrsim 200$, see figure 4(*b*,*c*) and p. 245. Both the subsonic $iAPG_{\beta_K=1.05}$ case in figure 5(*a*) and the supersonic $cFPG_{\beta_K=-0.18}$ case in figure 5(*c*) are characterized by positive wall-normal velocity components $\overline{v}/u_{\infty,0}$ at the top of the simulation domain, while the supersonic $cAPG_{\beta_K=0.69}$ case in figure 5(*b*) is characterized by negative $\overline{v}/u_{\infty,0}$. Note, however, that $\overline{v}/u_{\infty,0}$ is almost completely positive inside the boundary layer for the supersonic $cAPG_{\beta_K=0.69}$ case. This is caused by the strong deceleration of the supersonic flow where the subsonic displacing behaviour dominates the boundary layer; compare the red solid $\overline{v} = 0$ and black dash-dotted δ_{99}-lines.

Snapshots of the streamwise velocity component $u/u_e(x)$ are given in figures 6 and 7 for a subset of the simulation domain extracted at $Re_\tau = 490$ (FPG at $Re_\tau = 360$) to get an impression of the unsteady flow fields, see also figures 29 and 30. While the subsonic *iZPG* and $iAPG_{\beta_K=1.05}$ cases are depicted in figure 6(*a*,*b*), respectively, the

(a) Summary of simulation parameters for CPG TBLs

	Case	M_e	β_K	Re_θ	$Re_{\delta_{99}}$	Re_τ	Re_{δ_2}	H
(1)	iZPG (red)	0.50	0	1026–2308	8721–19 203	376–742	992–2233	1.57–1.52
(2)	iAPG$_{\beta_K=0.19}$ (red)	0.46–0.43	0.19	1193–2585	9435–20 058	395–764	1160–2523	1.58–1.52
(3)	iAPG$_{\beta_K=0.58}$ (red)	0.42–0.36	0.58	1552–3052	11 108–21 722	439–796	1519–3002	1.61–1.55
(4)	iAPG$_{\beta_K=1.05}$ (red)	0.38–0.33	1.05	1904–3444	12 812–22 903	480–798	1870–3398	1.64–1.60
(5)	cZPG (blue)	2.00	0	1026–2537	11 311–27 305	236–502	694–1716	3.30–3.22
(6)	cAPG$_{\beta_K=0.15}$ (blue)	1.93–1.77	0.15	1370–2977	14 365–29 500	300–611	949–2169	3.16–2.84
(7)	cAPG$_{\beta_K=0.42}$ (blue)	1.82–1.50	0.42	1526–3826	14 932–34 315	324–799	1095–3029	3.00–2.46
(8)	cAPG$_{\beta_K=0.55}$ (blue)	1.77–1.40	0.55	1566–4172	15 016–35 980	334–866	1141–3393	2.93–2.35
(9)	cAPG$_{\beta_K=0.69}$ (blue)	1.74–1.33	0.69	1629–4532	15 261–37 600	343–925	1200–3759	2.89–2.27
(10)	cFPG$_{\beta_K=-0.18}$ (cyan)	2.09–2.36	−0.18	1208–1994	13 983–24 429	270–369	792–1193	3.42–3.91

(b) Summary of numerical set-up information for CPG TBLs

	Case	$c_f \times 10^{-3}$	$(L_x \times L_y \times L_z)/\delta_{99,0}$	$N_x \times N_y \times N_z$	Δx^+	Δy_w^+	Δz^+
(1)	iZPG (red)	4.14–3.33	340 × 34 × 12π	2500 × 270 × 820	17.57–15.76	0.74–0.66	5.94–5.33
(2)	iAPG$_{\beta_K=0.19}$ (red)	3.84–3.14	340 × 34 × 12π	2500 × 270 × 820	16.05–13.67	0.67–0.57	5.43–4.62
(3)	iAPG$_{\beta_K=0.58}$ (red)	3.36–2.84	340 × 34 × 12π	2500 × 270 × 820	13.90–11.39	0.58–0.48	4.70–3.85
(4)	iAPG$_{\beta_K=1.05}$ (red)	2.98–2.54	340 × 34 × 12π	2500 × 270 × 820	12.30–9.94	0.52–0.42	4.16–3.36
(5)	cZPG (blue)	3.26–2.53	500 × 34 × 12π	5000 × 300 × 960	6.26–5.51	0.28–0.24	2.46–2.16
(6)	cAPG$_{\beta_K=0.15}$ (blue)	3.01–2.52	500 × 34 × 12π	5000 × 300 × 960	6.48–6.89	0.29–0.31	2.55–2.71
(7)	cAPG$_{\beta_K=0.42}$ (blue)	2.90–2.41	500 × 34 × 12π	5000 × 300 × 960	7.09–8.52	0.31–0.38	2.78–3.35
(8)	cAPG$_{\beta_K=0.55}$ (blue)	2.89–2.35	500 × 34 × 12π	5000 × 300 × 960	7.39–9.01	0.33–0.40	2.90–3.54
(9)	cAPG$_{\beta_K=0.69}$ (blue)	2.85–2.30	500 × 34 × 12π	5000 × 300 × 960	7.59–9.32	0.34–0.41	2.98–3.66
(10)	cFPG$_{\beta_K=-0.18}$ (cyan)	3.09–2.54	500 × 34 × 12π	5000 × 300 × 960	5.54–3.74	0.25–0.17	2.17–1.47

TABLE 3. Nearly incompressible cases with inflow Mach numbers of $M_{\infty,0} = 0.5$ are highlighted by red colour, supersonic cases with $M_{\infty,0} = 2.0$ by blue and cyan colours. Given parameters characterize the beginning and the end of the usable region where β_K is almost constant, see figure 10.
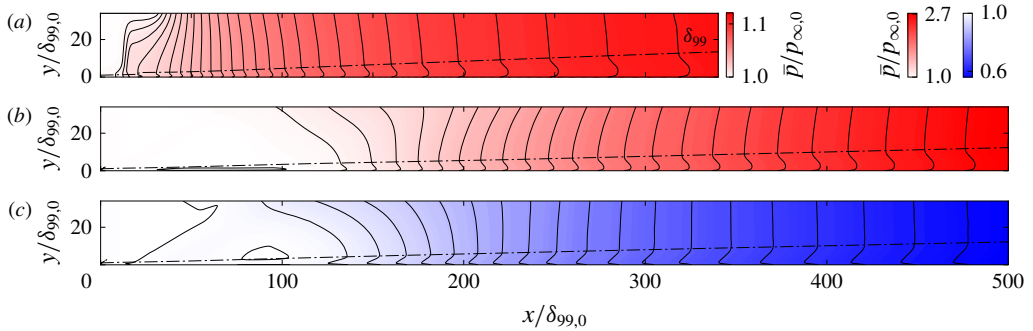
FIGURE 4. (Colour online) Mean-flow pressure field $\bar{p}/p_{\infty,0}$ for (*a*) the strongest subsonic $iAPG_{\beta_K=1.05}$ case, (*b*) the strongest supersonic $cAPG_{\beta_K=0.69}$ case and (*c*) the supersonic $cFPG_{\beta_K=-0.18}$ case.
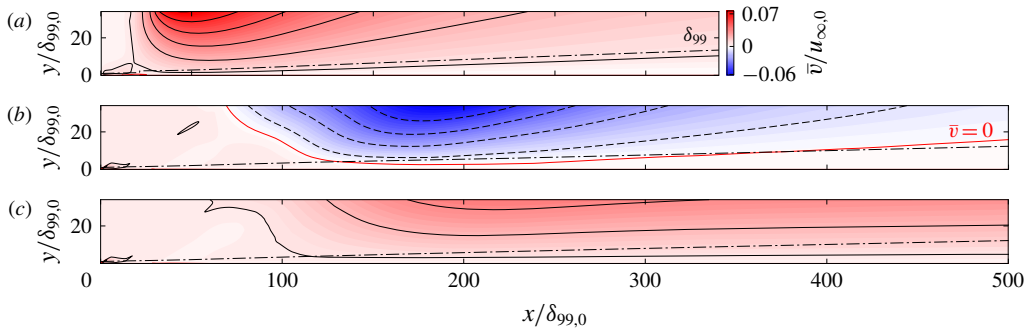

FIGURE 5. (Colour online) Mean-flow field of the wall-normal velocity component $\bar{v}/u_{\infty,0}$ for (*a*) the strongest subsonic $iAPG_{\beta_K=1.05}$ case, the strongest supersonic $cAPG_{\beta_K=0.69}$ case and the supersonic $cFPG_{\beta_K=-0.18}$ case.

supersonic $cAPG_{\beta_K=0.69}$, $cZPG$ and $cFPG_{\beta_K=-0.18}$ cases are depicted in figure 7(*a,b,c*), respectively. The time-averaged boundary-layer thickness $\bar{\delta}_{99}$ (only emphasized in the present plots with an overbar) and the instantaneous boundary-layer thickness δ_{99} are depicted as blue dash-dotted and solid lines, respectively. Grey iso-lines represent nine equidistantly distributed levels of the streamwise velocity component $u/u_e(x)$ between 0.1 and 0.9. Solely for the supersonic cases in figure 7, the instantaneous sonic line is depicted as a black bold solid line.

Compared with the incompressible *iZPG* case in figure 6(*a*), the subsonic APG case shows a coarsening of turbulent structures with increasing APG strength, see figure 6(*b*). For the supersonic cases in figure 7 the inverse trend is found, turbulent structures are refined for the APG case (figure 7*c*) and coarsened for the FPG (figure 7*a*) in comparison to the ZPG case (figure 7*b*). Whereas the sonic line is pushed to the wall for the supersonic FPG case, it is lifted for the APG case in the streamwise direction. Details will be discussed in the following sections.

Figures 8 and 9 illustrate iso-levels of the λ_2-criterion computed from the non-dimensionalized flow field $u_i = u_i/u_{\infty,0}$ with $\lambda_2 = -0.05\,u_e(x)/u_{\infty,0}$ for the previously discussed cases. Snapshots of the complete simulation domain are given in figures 29 and 30. In accordance with the instantaneous velocity fields given
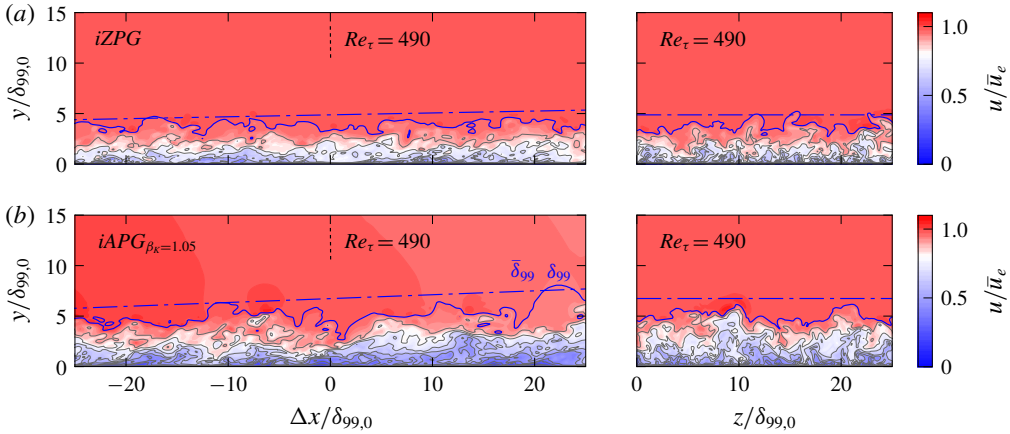
FIGURE 6. (Colour online) Snapshots of the streamwise velocity component $u/u_{\infty,0}$ for the (*a*) subsonic *iZPG* case and the (*b*) strongest subsonic *iAPG*$_{\beta_K=1.05}$ case at $Re_\tau = 490$. Left plots: *xy*-plane. Right plots: *zy*-plane.
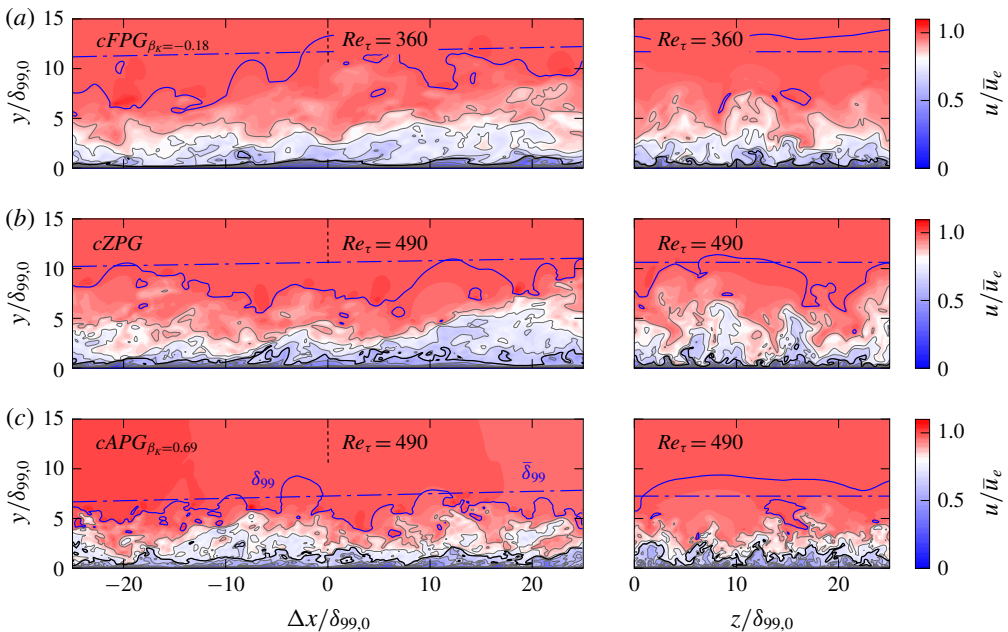

FIGURE 7. (Colour online) Snapshots of the streamwise velocity component $u/u_{\infty,0}$ for (*a*) the supersonic *cFPG*$_{\beta_K=-0.18}$ case, (*b*) the supersonic *cZPG* case and (*c*) the strongest supersonic *cAPG*$_{\beta_K=0.69}$ case at $Re_\tau = 490$ (FPG at $Re_\tau = 360$). Left plots: *xy*-plane. Right plots: *zy*-plane. The sonic line representing $M = 1$ is depicted as black bold line.

before, the λ_2-structures are thinned out for APGs in the subsonic and FPGs in the supersonic regime, and refined by APGs in the supersonic regime if compared to the respective ZPG case. A detailed investigation of compressible PG effects on the turbulent structures will be part of future studies.
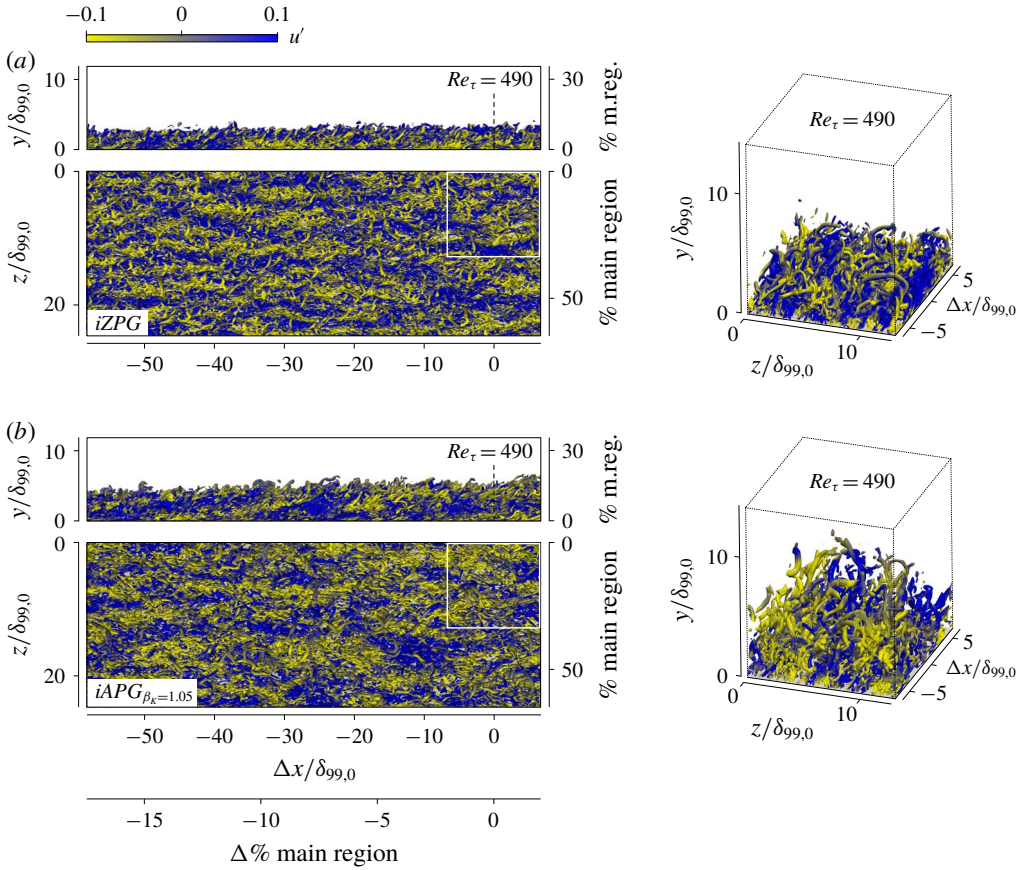
FIGURE 8. (Colour online) Snapshots of vortices by iso-surfaces of the λ_2-criterion with $\lambda_2 = -0.05 u_e(x)/u_{\infty,0}$ for (*a*) the subsonic *iZPG* case and (*b*) the strongest subsonic *iAPG*$_{\beta_K=1.05}$ case at $Re_\tau = 490$. Colour depicts the fluctuation amplitude of the streamwise velocity component $u'/u_{\infty,0}$. Left plots: subset of the simulation domain in top view. Right plots: close-ups of the white bordered regions in the left plots, see also figures 29 and 30.

3.2. *Boundary-layer characterization*

In this section the evolution of the most important boundary-layer quantities is described.

3.2.1. *Evaluation of the Rotta–Clauser parameter*

Both the kinematic and the compressible results of the Rotta–Clauser parameter $\beta_{(K)} = (\delta^*_{(K)}/\overline{\tau}_w)(dp_e/dx)$ are shown in figure 10, where the kinematic displacement thickness is $\delta^*_K = \int_0^{\delta_{99}}(1 - \overline{u}/u_e)\,dy$ and the compressible displacement thickness $\delta^* = \int_0^{\delta_{99}}(1 - (\overline{\rho}\,\overline{u})/(\rho_e u_e))\,dy$. It is shown in Part 2 of this study (Gibis *et al.* 2019) and by the DNS results discussed below that the β_K-parameter correctly characterizes the self-similar state of the compressible TBL and hence enables a comparison of PG influences between compressible and incompressible flows. The compressible definition β turns out to be less relevant because the compressible displacement thickness is not a good characterizing length scale for the outer part of the boundary
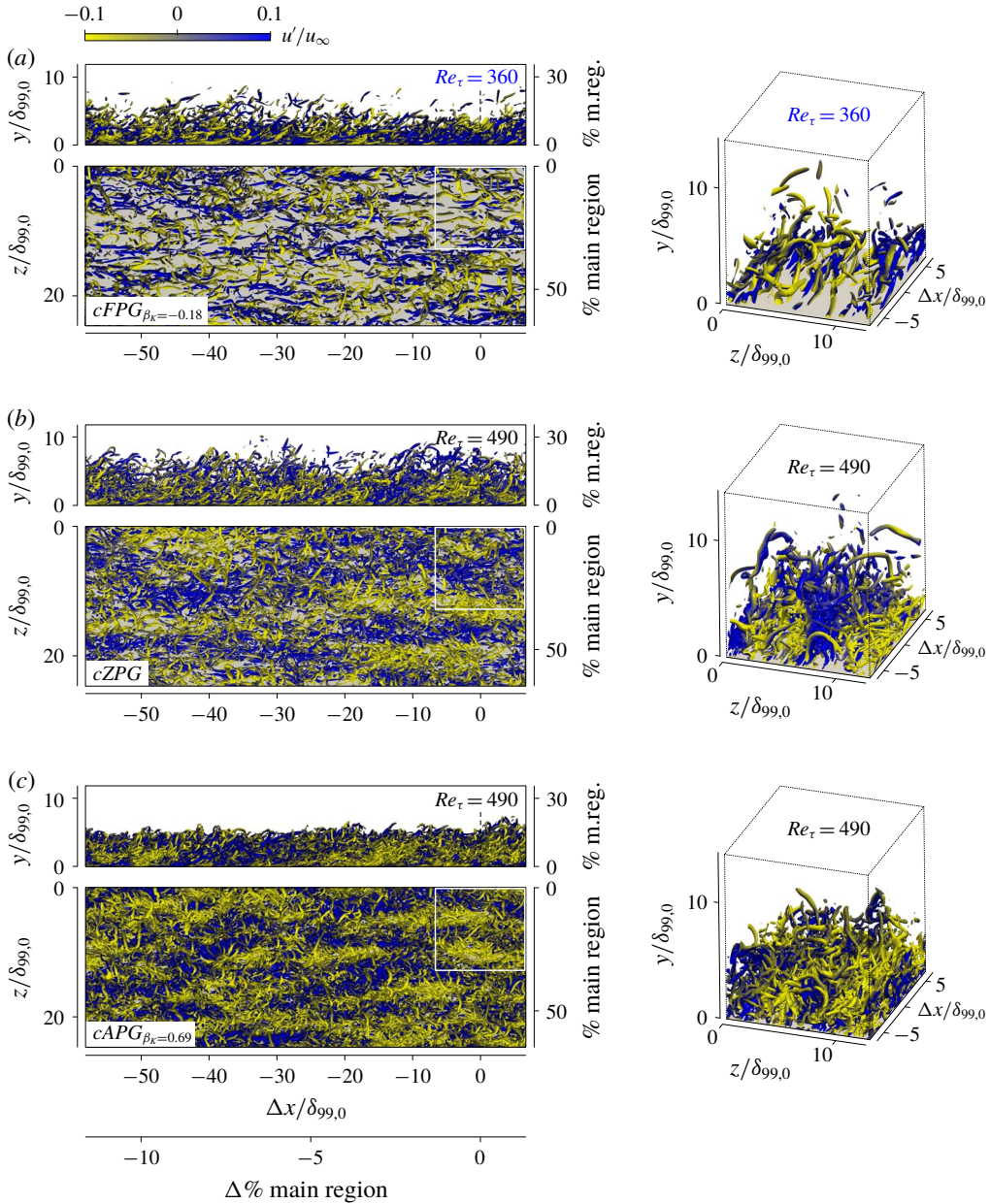
FIGURE 9. (Colour online) Snapshots of vortices by iso-surfaces of the λ_2-criterion with $\lambda_2 = -0.05 u_e(x)/u_{\infty,0}$ for (a) the supersonic $cFPG_{\beta_K=-0.18}$ case, (b) the supersonic $cZPG$ case and (c) the strongest supersonic $cAPG_{\beta_K=0.69}$ case at $Re_\tau = 490$ (FPG at $Re_\tau = 360$). Colour depicts the fluctuation amplitude of the streamwise velocity component $u'/u_{\infty,0}$ in the same representation as in figure 8, see also figures 29 and 30.

layer, as shown in Gibis *et al.* (2019). Since all simulations start with a ZPG region at the inflow (see § 2.4), an induction distance is needed before the individual $\beta_{(K)}$-values become approximately constant (grey dashed lines). Expressed in various Reynolds
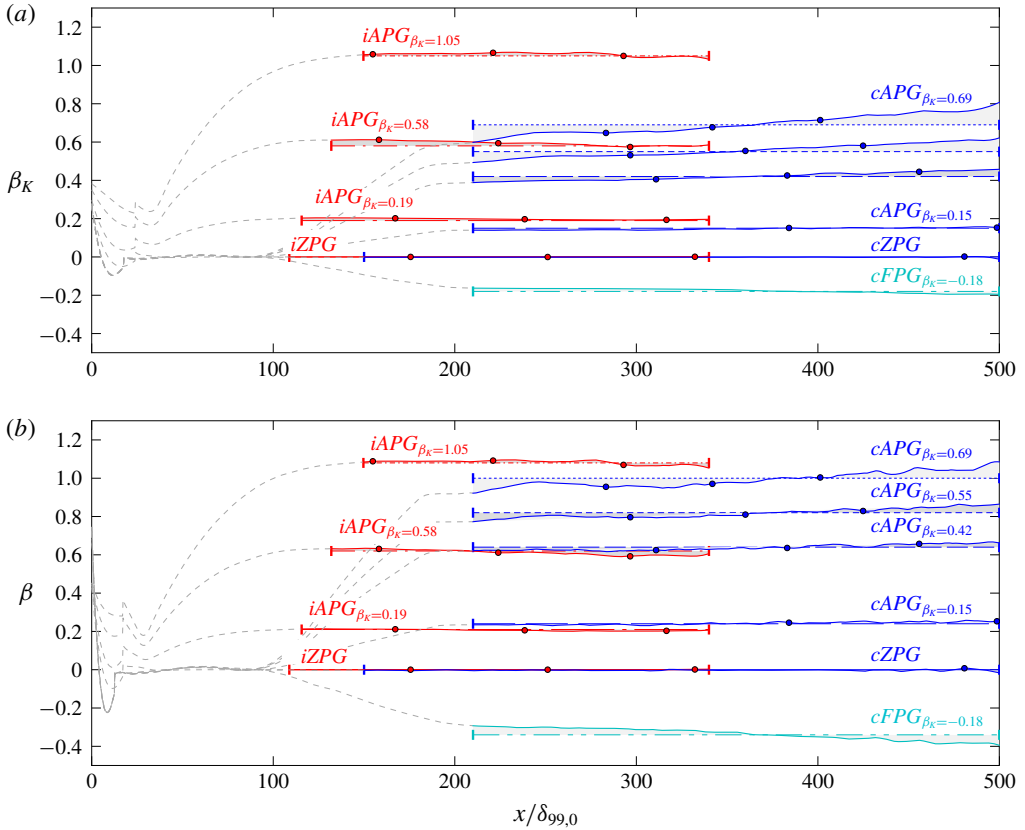
FIGURE 10. (Colour online) Clauser parameters $\beta_{(K)} = (\delta_{(K)}^*/\overline{\tau}_w)(\mathrm{d}p_e/\mathrm{d}x)$ for the computed results. Red lines represent the four subsonic cases, blue and cyan lines the six supersonic cases. Coloured horizontal lines represent curve fits of their solid line counterparts. Grey dashed lines represent induction regions, where $\beta_{(K)}$ is not yet constant. Expressed in various Reynolds numbers, both the start and the end of the coloured regions are summarized in table 3(a) for all cases.

numbers, the start and the end of the (almost) constant regions are summarized in table 3(a) for all cases.

An evaluation of the resulting $\beta_{(K)}$-values in figure 10 yields almost perfectly constant values for the subsonic APG cases, slightly rising values for the supersonic APG cases and slightly decreasing values for the supersonic FPG case. Due to the additional consideration of density variations in the wall-normal direction, β-values are increased compared to the β_K-values. As shown in the next section, δ_K^* and δ^* and thus also β_K and β are not proportional to each other in their streamwise evolution for the supersonic cases due to the varying influence of compressibility. The β_K-distributions are therefore slightly steeper compared to β. Whereas the subsonic cases are characterized by $\beta_K = 0.19$, 0.58 and 1.05, the supersonic cases yield $\beta_K = 0.15$, 0.42, 0.55 and 0.69 for the APG and $\beta_K = -0.18$ for the FPG case. The corresponding β-parameters are summarized in table 1.

Constant β_K-values mainly characterize the resulting mean flow but do not inevitably warrant perfect self-similarity of higher moments in the streamwise direction, since

influences resulting from history effects occurring in the induction sections cannot be excluded. Nevertheless, the achieved constancy of the distributions suggests an approximated state of local self-similarity for all PG cases for at least 50 average boundary-layer thicknesses $\delta_{99,av}$ but not exactly for $x \to \infty$. Detailed investigations are given in Gibis *et al.* (2019).

3.2.2. *Evolution of the boundary layer*

All supersonic APG cases follow the same qualitative trends; thus only the cases $cAPG_{\beta_K=0.42}$ and $cAPG_{\beta_K=0.69}$ are depicted.

Figure 11(*a*) illustrates the spatial evolution of the boundary-layer thickness $\delta_{99}/\delta_{99,0}$ and the wall-normal position of the sonic line $\delta_{SL}/\delta_{99,0}$ in green (line style in accordance with the boundary-layer thickness), the latter of which separates sub- and supersonic parts of the supersonic boundary-layer cases. The ratios of the boundary-layer thicknesses θ/δ_{99} and δ^*/δ_{99} are depicted in figures 11(*b*) and 11(*c*) for the sub- and supersonic cases, respectively. Solely for the supersonic cases, the ratios of the kinematic boundary-layer thicknesses are given in figure 11(*d*). For all three panels (*b,c,d*), results depicted by symbols belong to the *y*-axis located on the left-hand side of the plot; results depicted by lines belong to the *y*-axis located on the right-hand side of the plot.

For the quasi-incompressible cases, the boundary-layer thickens strongly with increasing APG strength (figure 11*a*) resulting in a maximum of twice the thickness of the ZPG case for the $iAPG_{\beta_K=1.05}$ case. When the pressure rises in subsonic flows, the velocity decreases more rapidly than the density increases. This results in a decompression of the streamtubes and thus an increase in the boundary-layer thickness (Spina, Smits & Robinson 1994).

Given in figure 11(*b*), the ratio of the momentum thickness θ/δ_{99} (red symbols, left *y*-axis) as well as the ratio of the displacement thickness δ^*/δ_{99} (red lines, right *y*-axis) are almost constant and thus almost proportional to each other in the streamwise direction, $\delta_{99} \propto \delta^* \propto \theta$. As a consequence, also the shape factor $H = \delta^*/\theta$ is almost constant as will be further discussed in § 3.3.1.

For the compressible, supersonic APG cases, the boundary-layer thickness $\delta_{99}/\delta_{99,0}$ is first reduced and then increased compared to the *cZPG* case and thus leads to an intersection point, see figure 11(*a*). Following Spina *et al.*'s (1994) argument, this counterintuitive behaviour is caused by the unique character of the supersonic boundary layer that consists of both sub- and supersonic regions. In contrast to the subsonic regions, the density increases more rapidly than the velocity decreases in supersonic regions for APGs, meaning that streamtubes are compressed in the supersonic part above the green sonic line and decompressed in the subsonic part below the sonic line. When the subsonic region of the boundary layer becomes large, which means that the sonic line is noticeably lifted off the wall (approximately for $M_\infty \lesssim 1.8$, cf. Spina *et al.* (1994)), the APG causes the boundary-layer thickness to increase and the wall shear stress to decrease. As given in table 3(*a*), the usable region of the $cAPG_{\beta_K=0.42}$ and $cAPG_{\beta_K=0.69}$ cases covers Mach-number ranges of $1.82 \geqslant M_e \geqslant 1.50$ and $1.74 \geqslant M_e \geqslant 1.33$, respectively, which approximately confirms the Spina *et al.*'s (1994) switch-over value of $M_\infty \lesssim 1.8$. For the compressible, supersonic $cFPG_{\beta_K=-0.18}$ case, the supersonic part dominates the boundary layer, which thus is thickened up in its spatial development compared to the *cZPG* case.

Discussing the momentum and displacement thickness distributions for all supersonic cases in figure 11(*c*) next, only the ratio of the momentum thickness θ/δ_{99} (symbols, left *y*-axis) is approximately constant in the streamwise direction.
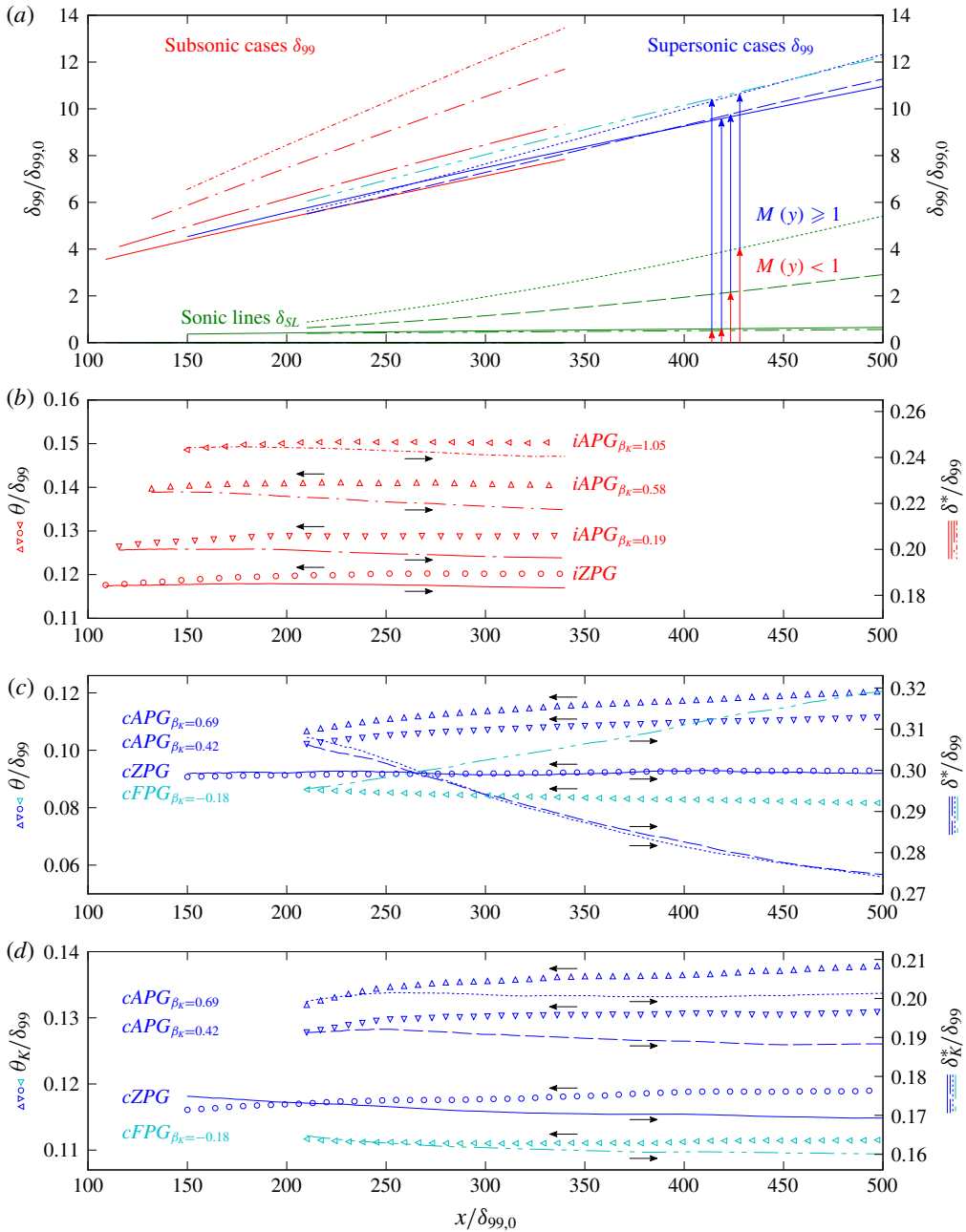
FIGURE 11. (Colour online) Boundary-layer values for regions of constant $\beta_{(K)}$. Subsonic and supersonic cases are coloured red and blue, respectively, the supersonic FPG case cyan. Depicted are (a) the boundary-layer thickness $\delta_{99}/\delta_{99,0}$ and the sonic lines in green solely for the supersonic cases; (b,c) the momentum thickness θ/δ_{99} (symbols, left y-axis) and the displacement thickness $\delta^*/\delta_{99,0}$ (lines, right y-axis) for the sub- and supersonic cases, respectively; (d) the kinematic momentum thickness θ_K/δ_{99} and the kinematic displacement thickness δ_K^*/δ_{99} solely for the supersonic cases.

The ratio of the displacement thickness δ^*/δ_{99} (lines, right y-axis) is strongly decreased for the APG and increased for the FPG cases, approximately leading to $\delta_{99} \propto \theta \not\propto \delta^*$. As a consequence also the shape factor H is not constant anymore for the compressible results as will be further discussed in § 3.3.1. An evaluation of the kinematic boundary-layer values in figure 11(d) can reproduce almost the same trends as for the nearly incompressible cases in figure 11(b), yielding again the approximate dependency of $\delta_{99} \propto \theta_K \propto \delta_K^*$ and thus the approximate constancy of $H_K = \delta_K^*/\theta_K$.

3.3. *Spatial evolution of averaged flow statistics*

This section provides the streamwise evolution of important mean-flow parameters as a function of the local Reynolds numbers Re_θ or Re_τ in the same representation as for the ZPG study in Wenzel *et al.* (2018*b*). It should be mentioned however that the interpretation of Re_θ may be difficult due to the non-intuitive development of the compressible PG TBL itself.

3.3.1. *Spatial evolution of mean-flow statistics*

Figures 12, 13 and 14 give the distribution of the skin-friction coefficient $c_f = 2\overline{\tau}_w/(\overline{\rho}_w u_e^2)$ with $\overline{\tau}_w = \overline{\mu \partial u/\partial y}_w \approx \overline{\mu}_w(\partial \overline{u}/\partial y)_w$, the skin-friction velocity Reynolds number $Re_\tau = \overline{\rho}_w u_\tau \delta_{99}/\overline{\mu}_w$ and the compressible (kinematic) shape factors $H_{(K)} = \delta_{(K)}^*/\theta_{(K)}$ as functions of the momentum-thickness Reynolds number $Re_{\theta_{(K)}} = \rho_e u_e \theta_{(K)}/\mu_e$. Additionally, as a function of the streamwise position $x/\delta_{99,0}$ and computed from $\overline{T}_{aw}/T_e = 1 + r(\gamma - 1)/2\,M_e^2$, the streamwise evolution of the recovery factor r is given in figure 15.

The c_f-distribution (figure 12) is supplemented by a black solid line representing a re-calibrated incompressible reference following $c_f = 0.0274\,Re_\theta^{-0.27}$ (re-calibration is based on the results from Wenzel *et al.* (2018*b*)). Note that the re-calibrated c_f-correlation also better represents the Schlatter & Örlü's (2010) incompressible dataset. Compressible references for $M_\infty = 0.5$ and 2.0 are computed from the van Driest II transformation (White 2006) and are depicted as grey dashed lines; see also Wenzel *et al.* (2018*b*). The Re_τ- and H_K-distributions are supplemented by the incompressible references according to Schlatter & Örlü (2010) and Chauhan, Monkewitz & Nagib (2009). Represented as grey dashed lines in figures 13 and 14, the compressible references are gained by shifting the incompressible correlations to fit the compressible ZPG results.

For the c_f-distributions in figure 12, both the sub- and the supersonic ZPG cases show excellent agreement with the compressibility transformed re-calibrated c_f-correlation. In accordance to the literature database, the c_f-distributions of the subsonic APG cases are shifted towards lower values for increasing APG strength. However, they almost follow the same slope as the subsonic ZPG case due to their (approximate) state of self-similarity. A comparison between the $iAPG_{\beta_K=1.05}$ case and the incompressible $\beta_K = 1.00$ case of Kitsios *et al.* (2017) (red circles) shows good agreement. The supersonic APG cases are difficult to interpret due to the strong coupling of PG and compressibility effects. According to Spina *et al.* (1994), the wall shear stress increases monotonically through the region of applied APGs for supersonic flows where the sonic line is close to the wall, meaning that $M_e \gtrsim 1.8$. The c_f-distribution, however, remains nearly constant due to the increase in $\rho_e u_e^2$. All supersonic APG cases are therefore in a comparable c_f-range for $Re_\theta \lesssim 1700$ where local Mach numbers are about $M_e \approx 1.8$, see table 3(a). For higher Reynolds numbers,
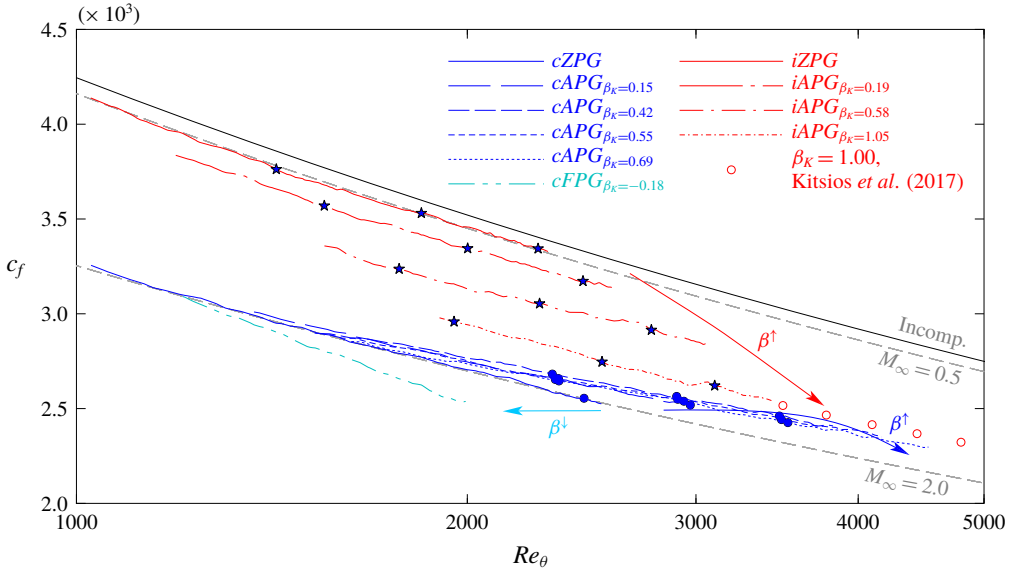
FIGURE 12. (Colour online) Skin-friction coefficient c_f as function of Re_θ. The incompressible, re-calibrated correlation (black solid line) is given by $c_f = 0.0274\,Re_\theta^{-0.27}$, the compressible one by the van Driest II transformation (grey dashed lines, see White (2006)).
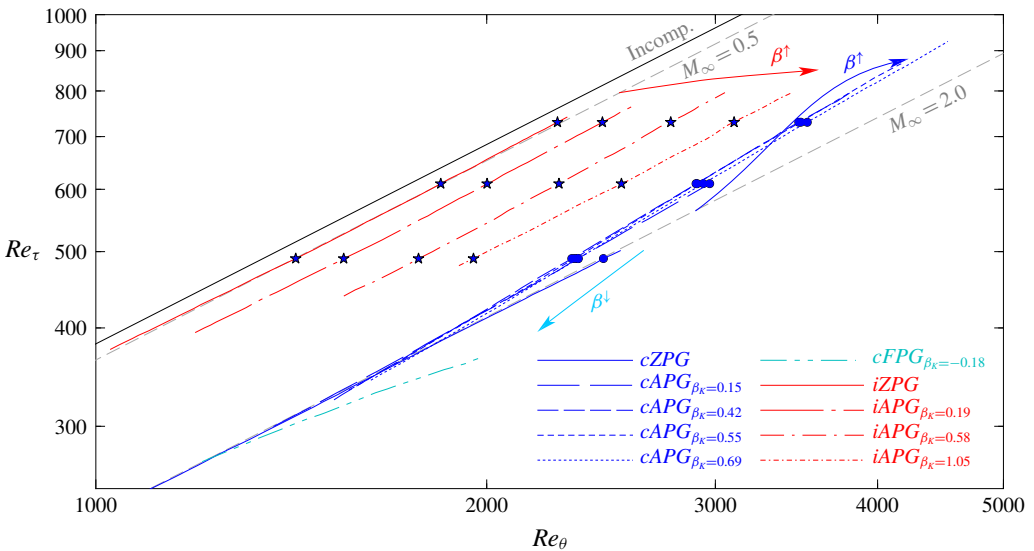

FIGURE 13. (Colour online) Skin-friction velocity Reynolds number Re_τ as function of Re_θ. The incompressible correlation is given by $Re_\tau = 1.13\,Re_\theta^{0.843}$ (black solid line, see Schlatter & Örlü (2010)), the compressible ones by the simple shift of the incompressible correlation (grey dashed lines).
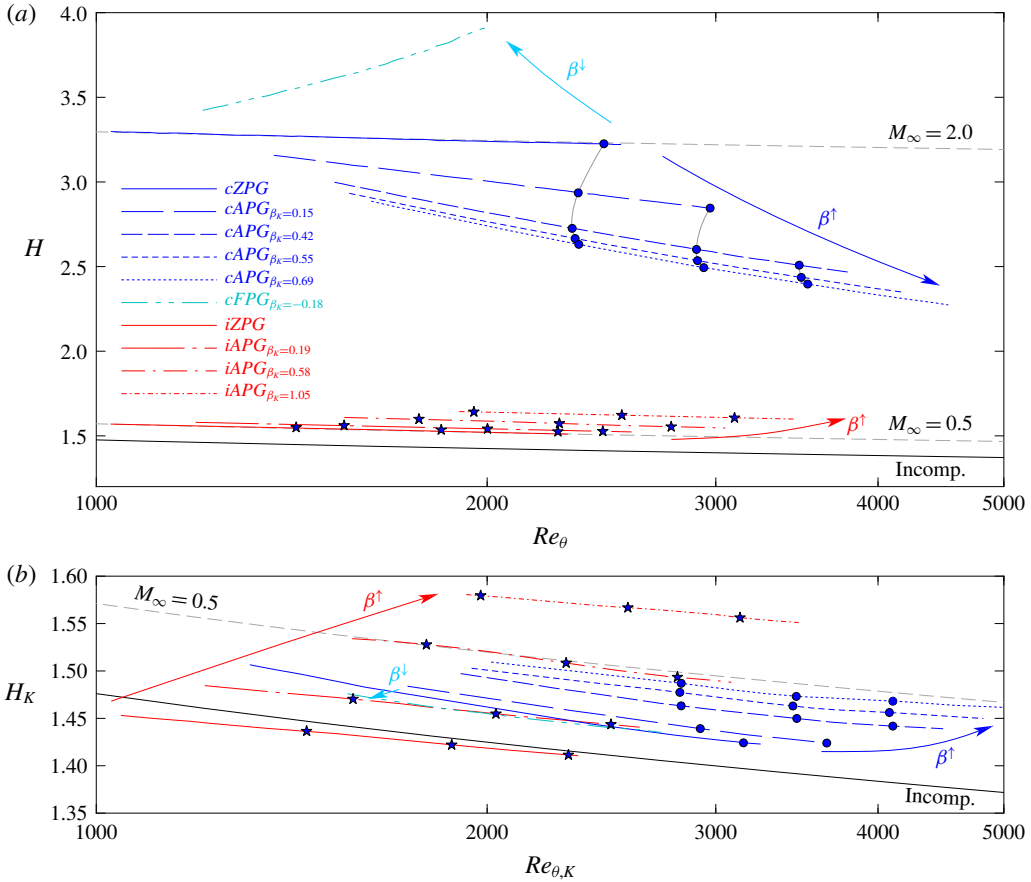
(a) [graph with axis label H on vertical axis, Re_θ on horizontal axis]

Legend:
- cZPG
- $cAPG_{\beta_K=0.15}$
- $cAPG_{\beta_K=0.42}$
- $cAPG_{\beta_K=0.55}$
- $cAPG_{\beta_K=0.69}$
- $cFPG_{\beta_K=-0.18}$
- iZPG
- $iAPG_{\beta_K=0.19}$
- $iAPG_{\beta_K=0.58}$
- $iAPG_{\beta_K=1.05}$

$M_\infty = 2.0$
$M_\infty = 0.5$
Incomp.

(b) [graph with axis label H_K on vertical axis, $Re_{\theta,K}$ on horizontal axis]

$M_\infty = 0.5$
Incomp.

FIGURE 14. (Colour online) (*a*) Shape factor H and (*b*) kinematic shape factor H_K as a function of Re_θ and $Re_{\theta,K}$, respectively. The incompressible correlation is given as the shape of the integrated incompressible composite profiles (Chauhan *et al.* 2009). The compressible references are gained by a simple shift of the incompressible correlation.

compressibility effects become weaker due to a decrease of the local Mach number and the c_f-distributions are increasingly dominated by PG effects. Since the PG is stronger for the $cAPG_{\beta_K=0.69}$ case compared to the $cAPG_{\beta=0.42}$ case, for instance, the c_f-distribution of the $cAPG_{\beta_K=0.69}$ case is lower compared to the $cAPG_{\beta_K=0.42}$ case. The interpretation of the supersonic FPG is opposite: compressibility effects (decreasing c_f) dominate the PG effect (increasing c_f), which thus yields a steeper downwards running c_f-slope compared to the ZPG case.

The interpretation of the Re_τ-distributions in figure 13 follows the same arguments as for the c_f-distribution due to their mutual dependency on the non-dimensional wall shear stress. Subsonic APG cases can be gained by shifting the ZPG results to higher Re_θ- and slightly increased Re_τ-values. The supersonic APG and FPG cases show a consistent behaviour as the c_f-distributions discussed before. Note that the Re_τ-distributions for the supersonic APG cases are slightly curved in the double-logarithmic representation since they have to converge towards the incompressible distributions when decelerated to almost incompressible Mach numbers.
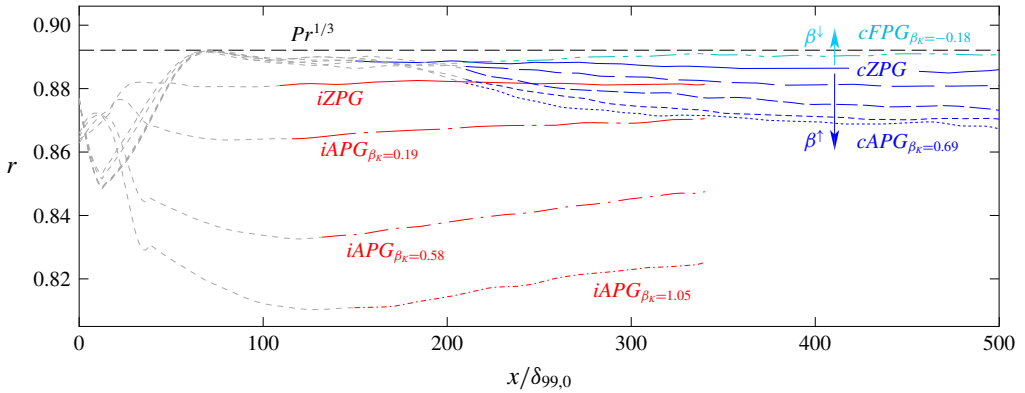
FIGURE 15. (Colour online) Distribution of the recovery factor r as function of streamwise position $x/\delta_{99,0}$. Red coloured lines represent the subsonic cases, blue and cyan lines the supersonic cases. Grey dotted lines denote the induction regions where $\beta_{(K)}$ is not yet constant, see figure 10.

Calculated in its compressible formulation, the shape-factor distribution H (figure 14a) is more influenced by compressibility effects than by PG effects, which makes the interpretation of the compressible results more unambiguous. Whereas the subsonic APG cases again seem to be obtainable by shifting the ZPG distribution towards higher values, the shape factors of the supersonic APG cases become significantly smaller in the streamwise direction caused by the substantial decrease in the local Mach number. For instance, the Mach number of the $cAPG_{\beta_K=0.69}$ case is lower at the end of the simulation domain than the Mach number of the $cAPG_{\beta_K=0.55}$ case, and its shape factor is lower. For the supersonic FPG case, the reversed argument holds. When calculated without taking density variations in the wall-normal direction into account, compressibility influences are almost eliminated for the kinematic shape-factor distributions H_K in figure 14(b). However, a quantitative comparison between sub- and supersonic cases seems not to be reasonable, see also figure 11(d). But especially for the self-similarity analysis in Gibis *et al.* (2019), the coalescence of sub- and supersonic kinematic shape factors will be utilized in the definition of appropriate length scales defining the state of the compressible PG TBL.

The recovery factor r is expected to be constant in the streamwise direction for self-similar flows, see Gibis *et al.* (2019), but not necessarily with the same value for different β_K-cases. Figure 15 shows the various curves compared to the often used ZPG reference value $r = Pr^{1/3} \approx 0.892$; constancy of r might be interpreted as an indicator for the state of self-similarity reached by the thermal boundary layer.

For the subsonic cases, an increasing APG means lower recovery factor values, with slightly rising trends in the streamwise direction. Whereas its value is approximately equal to $r \approx 0.88$ for the *iZPG* case, its value is about $r \approx 0.82$ for the strongest APG case and thus decreased by 7%. Note that the calculation of r for low Mach numbers gets very sensitive and does not make sense for zero Mach number.

Although being much less influenced by PGs compared to the subsonic cases, similar behaviour is observed for the supersonic cases. Whereas r is decreased by approximately 2% for the strongest supersonic APG case compared to the ZPG case, the FPG case value is increased by approximately 1%. Compared to the subsonic cases, r is much more constant in the streamwise direction for $x/\delta_{99,0} \gtrsim 300$, but needs
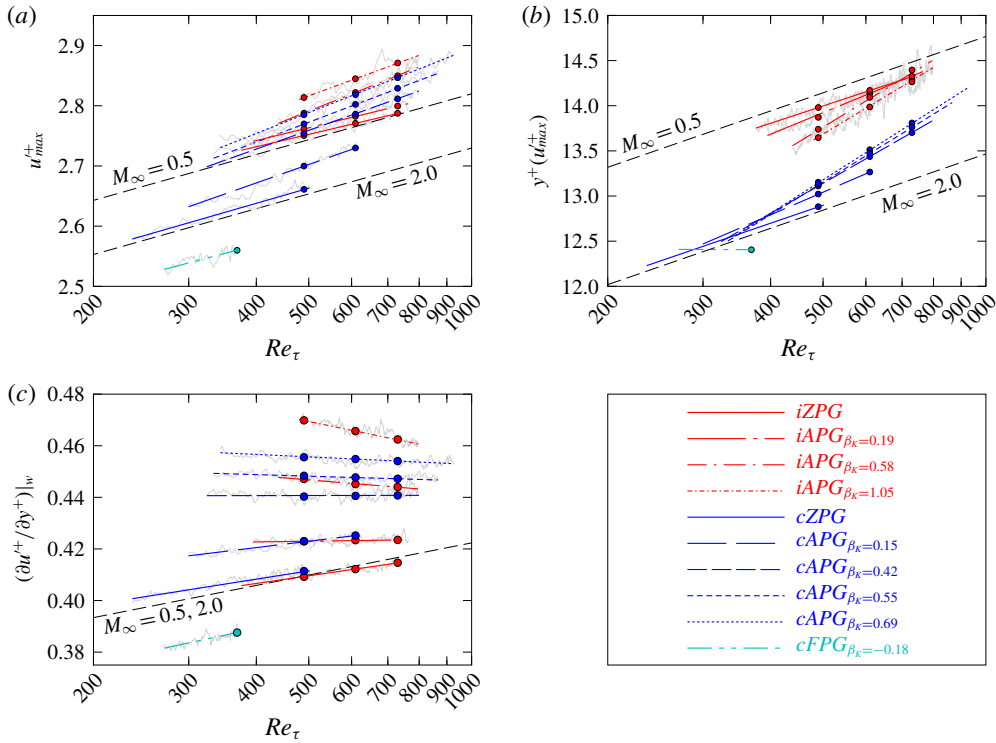
FIGURE 16. (Colour online) Near-wall behaviour of the streamwise velocity fluctuation $u'^+ = \sqrt{\overline{u'^2}}/u_\tau$ in inner scaling versus Re_τ (cf. Schlatter & Örlü 2010). (*a*) Peak value of the wall-near maximum u'^+_{max}, (*b*) the wall-normal position of the maximum $y^+\left(u'^+_{max}\right)$ and (*c*) the wall slope $(\partial u'^+/\partial y^+)|_w$. Black dashed lines are references for the ZPG cases taken from Wenzel *et al.* (2018*b*).

an induction distance of approximately $\Delta x/\delta_{99,0} \approx 100$ to reach the constant state. It is therefore expected that the thermal boundary layer requires more time/space to fully adapt to the self-similar state. The effects of the elongated induction distance on self-similarity of local mean-flow profiles are further discussed in Gibis *et al.* (2019).

3.3.2. *Spatial evolution of averaged fluctuation statistics*

The peak value u'^+_{max} of the Reynolds fluctuations in the streamwise direction $u'^+ = \sqrt{\overline{u'^2}}/u_\tau$ and their wall-normal position $y^+(u'^+_{max})$ are given in figure 16(*a,b*), respectively. The wall slope $(\partial u'^+/\partial y^+)|_w$ is given in figure 16(*c*). All distributions are plotted versus Re_τ. In order to emphasize their spatial trends, all data (grey solid lines in the background) are approximated by a coloured linear regression. (The linear slopes are only rough approximations which are not expected to hold for higher Reynolds numbers. The supersonic cases, for instance, are decelerated to the incompressible regime and thus have to converge to the incompressible references.) Taken from Wenzel *et al.* (2018*b*), black dashed lines represent references for both ZPG cases.

For the subsonic cases in figure 16(*a*) first, the peak value of the streamwise velocity fluctuation u'^+_{max} is increased by up to 10 % in the investigated β_K- and

Re_τ-range for the strongest APG case. The slope of the linear regression is slightly increased. For the supersonic APG cases this shift is larger, since both the effect of a decreasing Mach number in the streamwise direction and APGs supplement each other. With opposing argumentation, a contrary behaviour is found for the supersonic FPG case.

For the subsonic cases, the wall-normal position of the fluctuations' maximum value $y^+(u'^+_{max})$ in figure 16(*b*) is shifted towards the wall for lower and away from the wall for higher Reynolds numbers. For increasing APG strength, the slope of the linear regressions is increased. For the supersonic PG cases, both the effects of varying Mach number in the streamwise direction and PGs are opposed to each other, which leads to comparable distributions for the $cAPG_{\beta_K=0.55}$ and $cAPG_{\beta_K=0.69}$ cases for instance. Globally, the maxima are shifted away from the wall for Re_τ larger than 350.

The wall slope in figure 16(*c*) shows a comparable behaviour for both sub- and supersonic cases, although the slopes of the supersonic cases are somewhat lower compared to the subsonic ones. More details will be discussed in the next section.

4. Results for the transformed, local flow fields

Sub- and supersonic PG cases are not necessarily assumed to directly compare since compressibility transformations – which would enable a direct quantification of PG influences by eliminating the effect of compressibility – might be often only expected to be 'valid by definition' for the strict case of ZPGs. To prove the applicability of both Morkovin's scaling/hypothesis and van Driest's transformation for CPG TBLs, their underlying assumptions are shortly introduced and evaluated in the first part of this section. On this basis, the streamwise mean-flow velocity profiles and Reynolds fluctuations are summarized for all PG cases.

4.1. *Discussion of the validity of compressibility transformations*

According to Morkovin (1961), the Reynolds fluctuations $\overline{u'_i u'_j}$ are (almost) invariant with respect to the Mach number M, if scaled with the wall-normal density ratio $\overline{\rho}/\overline{\rho}_w$ and the skin-friction velocity u_τ^2

$$\frac{\overline{\rho}}{\overline{\rho}_w} \frac{\overline{u'_i u'_j}}{u_\tau^2} \neq f(M). \tag{4.1}$$

This is generally known as Morkovin's scaling. Depending on the particular argumentation, this scaling uses, among others, the assumption that the total stress $\overline{\tau}_t = \overline{\mu}(\mathrm{d}\overline{u}/\mathrm{d}y) - \overline{\rho u'v'}$ is constant and equal to $\overline{\tau}_w$ in the inner region of the boundary layer (cf. Smits & Dussauge (2006) and Cebeci & Bradshaw (1984) for instance). For PG cases, however, the shear-stress distribution varies near the wall to first order by $\overline{\tau}_t \approx \overline{\tau}_w + (\mathrm{d}p_e/\mathrm{d}x)y$ and thus directly connects the total shear-stress distribution to the streamwise pressure gradient (White 2006; Skote *et al.* 1998). Nevertheless, by assuming a constant stress region within the inner 20 per cent of the boundary layer if the PG is weak, see Cebeci & Bradshaw (1984), basic compressible principles like Morkovin's scaling are often assumed to approximately hold for the compressible PG regime.

Implicitly depending on Morkovin's scaling, the derivation of van Driest's transformation as given by

$$\mathrm{d}\overline{u}_{VD} = \left(\frac{\overline{\rho}}{\overline{\rho}_w}\right)^{1/2} \mathrm{d}\overline{u}, \tag{4.2}$$

which additionally depends on the validity of the inner layer mixing length $l_m^2 = -\overline{u'v'}/(\partial \overline{u}/\partial y)^2$ which departs in the outer layer from its inner value even for ZPG cases, see Wenzel *et al.* (2018*b*), for instance. Hence, in contrast to Morkovin's scaling, the van Driest transformation is not expected to entirely eliminate compressibility effects in the outer layer at all, as the mixing length is also expected to be influenced by PGs. Following the interpretation of Cebeci & Bradshaw (1984), the van Driest transformed velocity profile

$$\overline{u}_{VD}^+ = \frac{1}{k} \ln y^+ + C + \frac{\Pi}{k} \, w\left(\frac{y}{\delta_{99}}\right) \quad (4.3)$$

thus only can be interpreted as an adequate solution of compressible PG TBLs, if its parameters C and Π are calibrated to the particular case by using compressible reference data. The van Driest transformation itself only gives the framework of how this solution has to look. Also, the variation of u_τ, C and Π in the streamwise x-direction will not generally correspond to any realizable incompressible boundary layer. Hence it may not be possible to choose a pressure distribution $p_e(x)$ for an incompressible flow that will reproduce the same velocity profile as in the compressible flow at each x-position. Cebeci & Bradshaw (1984) therefore concluded that only 'the spirit of van Driest's transformation, although not in its details, would be retained if compressible boundary layers were calculated using the mixing-length formula'.

In the following, mainly the plausibility of Morkovin's scaling – and thus implicitly the plausibility of van Driest's transformation in the inner region – is discussed by evaluation of the mean shear-stress distributions. Further insight into the coupling between compressibility and PG effects are given afterwards by discussing the wall-normal distributions of the mean-flow pressure and pressure-fluctuation fields.

4.1.1. *Shear-stress distributions*

According to Guarini *et al.* (2000), the total shear stress $\overline{\tau}_t$ writes

$$\underbrace{\overline{\tau}_t}_{total\,stress} = \underbrace{\overline{\mu}\frac{\partial \overline{u}}{\partial y}}_{mean\,stress} - \underbrace{\overline{\rho u''v''}}_{turbulent\,stress} + \underbrace{\overline{\mu'\left(\frac{\partial u'}{\partial y} + \frac{\partial v'}{\partial x}\right)}}_{stress\,correlation}, \quad (4.4)$$

where f'' denotes fluctuations about the Favre average $\tilde{f} = \overline{\rho f}/\overline{\rho}$ for an unsteady quantity f. Normalized by the wall shear stress $\overline{\tau}_w = \overline{\rho}_w u_\tau^2$, the mean shear stress, the turbulent stress and the total stress are given in figure 17(*a*–*c*) for all cases, respectively. The distribution of the shear-stress correlation is almost zero and therefore not considered in the following. Based on the first-order expansion of the total shear-stress distribution $\overline{\tau}_t \approx \overline{\tau}_w + (\mathrm{d}p_e/\mathrm{d}x)y$, the pressure-corrected total shear-stress distribution $\overline{\tau}_{t,pc} = \overline{\tau}_t - (\mathrm{d}p_e/\mathrm{d}x)y$ is given in figure 17(*d*). All data are extracted at $Re_\tau = 490$ except for the supersonic FPG case where data are extracted at $Re_\tau = 360$.

Given in figure 17(*a*), the mean shear-stress distribution is almost constant at the wall for all cases and only slightly influenced by both compressibility and PG effects in the buffer layer between the viscous sublayer and the log layer at $3 \lesssim y^+ \lesssim 50$. For the subsonic cases, the mean shear-stress distributions are slightly decreased
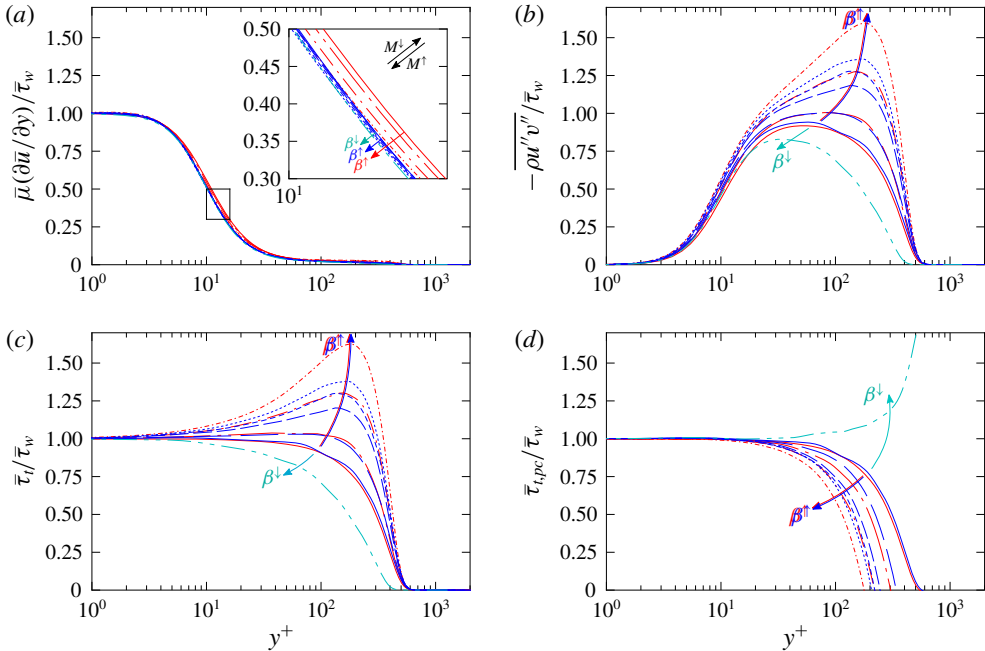
FIGURE 17. (Colour online) Comparison of (*a*) the mean shear stress $\overline{\mu}(\partial\overline{u}/\partial y)/\overline{\tau}_w$, (*b*) the turbulent shear stress $-\overline{\rho u''v''}/\overline{\tau}_w$, (*c*) the total shear stress $\overline{\tau}_t$ and (*d*) the pressure-corrected total shear stress $\overline{\tau}_{t,pc} = \overline{\tau}_t - (\mathrm{d}p_e/\mathrm{d}x)y$. Supersonic FPG data are extracted at $Re_\tau = 390$, other data at $Re_\tau = 490$. Red: —— $iZPG$, ——·· $iAPG_{\beta_K=0.19}$, —·— $iAPG_{\beta_K=0.58}$, —·—·— $iAPG_{\beta_K=1.05}$. Blue: —— $cZPG$, ——— $cAPG_{\beta_K=0.15}$, ——·- $cAPG_{\beta_K=0.42}$, ––––– $cAPG_{\beta_K=0.55}$, ------ $cAPG_{\beta_K=0.69}$. Cyan: —·–- $cFPG_{\beta_K=-0.18}$.

with increasing APG strength. The supersonic cases are almost identical since effects of decreasing Mach number (increasing) and increasing effect of APG (decreasing) cancel each other.

The non-dimensional turbulent stresses $-\overline{\rho u''v''}/\overline{\tau}_w$ in figure 17(*b*) are strongly influenced by PG effects over the entire boundary layer for both sub- and supersonic Mach numbers. For increasing APG strength a peak rises in the outer region whereas the distributions are reduced for FPGs. In contrast to the mean-flow distributions, the turbulent stresses are also noticeably influenced in the near-wall region.

Computed as the sum of (*a*) and (*b*), the total shear-stress distributions in figure 17(*c*) are constant for the sub- and supersonic ZPG cases up to approximately 30–40 wall units above the wall and virtually identical. For both the sub- and supersonic PG cases the distributions are increased with distance to the wall for APG cases ($\mathrm{d}p/\mathrm{d}x > 0$) and decreased for the FPG case ($\mathrm{d}p_e/\mathrm{d}x < 0$) by following $\mathrm{d}\overline{p}/\mathrm{d}x = \partial\overline{\tau}_t/\partial y$ (Smits & Dussauge 2006). If the PG term ($\mathrm{d}p_e/\mathrm{d}x)y$ is subtracted from the total shear-stress distributions as given in figure 17(*d*), the constant stress region near the wall is regained for all PG cases. Since the mean shear stresses in (*a*) are almost unaffected by PGs and almost constant at the wall, PG effects included in the total shear-stress distributions by ($\mathrm{d}p_e/\mathrm{d}x)y$ are mainly balanced by the turbulent stresses at the wall (Smits & Dussauge 2006).

A comparison between the total shear-stress distributions for the sub- and supersonic PG cases in (*c*) shows an almost complete agreement between the $iAPG_{\beta_K=0.19}$ and $cAPG_{\beta_K=0.15}$ cases and the $iAPG_{\beta_K=0.58}$ and $cAPG_{\beta_K=0.55}$ cases. If incompressible and compressible PG cases are chosen to be characterized by the same kinematic Rotta–Clauser parameter β_K, cases are thus constructed with the same total shear-stress distributions. This in turn implies the Mach-number invariance of $\overline{\tau}_t/\overline{\tau}_w$ for compressible PG cases,

$$\left.\frac{\overline{\tau}_t}{\overline{\tau}_w}\right|_{PG} = f(PG) \neq f(M). \tag{4.5}$$

As long as differences in the mean shear-stress distributions are not too large, also the turbulent stresses $-\overline{\rho u'' v''}/\overline{\tau}_w$ are invariant to the Mach number, which further verifies the applicability of Morkovin's scaling for the present compressible PG cases

$$\left.\frac{-\overline{\rho u'' v''}}{\overline{\tau}_w}\right|_{PG} \approx \frac{\overline{\rho}}{\overline{\rho}_w} \left.\frac{-\overline{u'v'}}{u_\tau^2}\right|_{PG} = f(PG) \neq f(M). \tag{4.6}$$

4.1.2. *Pressure distributions*

From the shear-stress distributions discussed in the previous section, compressibility and PG effects have been found to be almost uncoupled for the $-\overline{u'v'}$ fluctuations. If it is further assumed that Morkovin's scaling also holds for the $\overline{v'^2}$-fluctuations, meaning that $(\overline{\rho}/\overline{\rho}_w)(\overline{v'^2}/u_\tau^2) \neq f(M)$, the non-dimensionalized y-momentum equation of the two-dimensional turbulent boundary-layer equations

$$\frac{p_{e\approx w} - \overline{p}}{\overline{\rho}_w u_\tau^2} = \frac{\overline{\rho}}{\overline{\rho}_w} \frac{\widetilde{v''^2}}{u_\tau^2} \neq f(M) \tag{4.7}$$

implies that the pressure distributions $(p_{e\approx w} - \overline{p})/(\overline{\rho}_w u_\tau^2) = (p_{e\approx w} - \overline{p})^+$ of corresponding PG cases are comparable for different Mach numbers. (The index '$e \approx w$' should emphasize that the pressure p can be evaluated both at the edge of the boundary layer or at the wall.) If it is also assumed that comparable mean pressure distributions yield comparable pressure fluctuations $p'^+ = \sqrt{\overline{p'^2}}/\overline{\tau}_w$, also their wall-normal distributions should be comparable for corresponding β_K-cases at different Mach numbers.

The mean-pressure and the pressure-fluctuation distributions are depicted in figure 18(*a,b*), respectively. The mean-pressure fields are extracted at $Re_\tau = 490$, where data of all cases except for the FPG case are available. Due to the SEM inflow boundary condition, the wall pressure fluctuations are increased by about ten per cent in the inflow region of the simulation domain for the subsonic cases. These initial disturbances have decayed after about half of the simulation domain, such that reliable pressure-fluctuation distributions are only available for the second half of the domain for the subsonic cases. The development of other flow quantities like density or temperature fluctuations are unaffected by the inflow boundary condition, see Wenzel *et al.* (2018*b*). For the supersonic cases, pressure fluctuations are almost immediately comparable to reference data near the inflow of the domain, as the general pressure-fluctuation level is higher inside the supersonic boundary layer. Hence, the pressure-fluctuation profiles given in figure 18(*b*) are extracted at $Re_\tau = 730$ to allow a meaningful comparison. Panel (*b*) is supplemented by incompressible and
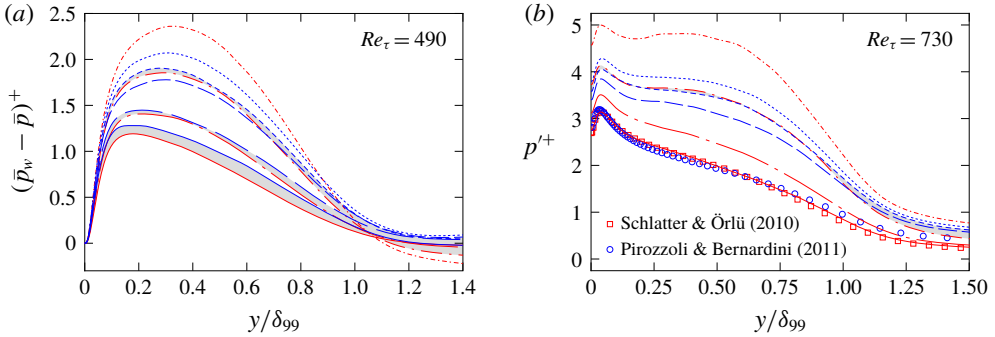
FIGURE 18. (Colour online) (*a*) Mean-flow pressure distribution $(\bar{p} - \bar{p}_w)^+ = (\bar{p} - \bar{p}_w)/\bar{\tau}_w$ at $Re_\tau = 490$ and (*b*) pressure fluctuations $p'^+ = \sqrt{\overline{p'^2}}/\bar{\tau}_w$ at $Re_\tau = 730$. ZPG references: Schlatter & Örlü (2010) at $Re_\tau = 830$ (incompressible), Pirozzoli & Bernardini (2011) at $Re_\tau = 840$ ($M_\infty = 2.0$). Red: —— $iZPG$, ——·· $iAPG_{\beta_K=0.19}$, —·— $iAPG_{\beta_K=0.58}$, –·–·– $iAPG_{\beta_K=1.05}$. Blue: —— $cZPG$, ——– $cAPG_{\beta_K=0.15}$, ——· $cAPG_{\beta_K=0.42}$, ––––– $cAPG_{\beta_K=0.55}$, ······ $cAPG_{\beta_K=0.69}$. Cyan: —–·· $cFPG_{\beta_K=-0.18}$.

compressible ZPG reference data taken from Schlatter & Örlü (2010) at $Re_\tau = 830$, and Pirozzoli & Bernardini (2011) at $Re_\tau = 840$ and $M_\infty = 2.0$, respectively.

For increasing APG strength, the peak of the mean pressure distributions is lifted away from the wall and the profiles become fuller, see (*a*). The distribution of the subsonic ZPG case is slightly lower compared to the supersonic ZPG case. If evaluated at comparable β_K-values, the distributions are almost identical for the sub- and supersonic APG cases as emphasized by the grey shaded regions. The pressure fluctuations in (*b*) are virtually unaffected by compressibility effects for the ZPG cases as already shown in Wenzel *et al.* (2018*b*) for instance, yielding an excellent agreement of the subsonic ZPG case and the incompressible and compressible ZPG references. With increasing APG strength, the fluctuation intensity increases for both sub- and supersonic cases but still remains almost identical for cases of comparable β_K, yielding

$$\left. \frac{\overline{p'^2}}{\bar{\rho}_w u_\tau^2} \right|_{PG} = f(PG) \neq f(M). \tag{4.8}$$

4.1.3. *Wall-normal velocity fluctuations $\overline{v'^2}$*

Based on the previous argumentation, the close agreement between the mean-pressure distributions of sub- and supersonic counterparts with similar β_K has been implied by the assumed validity of Morkovin's scaling for the wall-normal velocity fluctuations $\overline{v'^2}$ (or *vice versa*). To verify the accuracy of the simplified *y*-momentum equation of the turbulent boundary-layer equations for compressible PG cases (4.7) and thus the success of Morkovin's scaling for the wall-normal velocity fluctuations $\overline{v'^2}$, these are given both in unscaled $\sqrt{\overline{v'^2}}/u_\tau$ and Morkovin-scaled $\sqrt{\bar{\rho}/\bar{\rho}_w}\sqrt{\overline{v'^2}}/u_\tau$ representation in figure 19(*a,b*), respectively. For better comparability, only sub- and supersonic cases with similar β_K-values are considered. All results are extracted at the three Reynolds-number values $Re_\tau = 490$, 610 and 730, diagonally staggered in ascending order. Represented as circled symbols in (*b*), some pressure distributions $\sqrt{(\bar{p}_w - \bar{p})/(\bar{\rho}_w u_\tau^2)}$ are additionally given for selected cases.
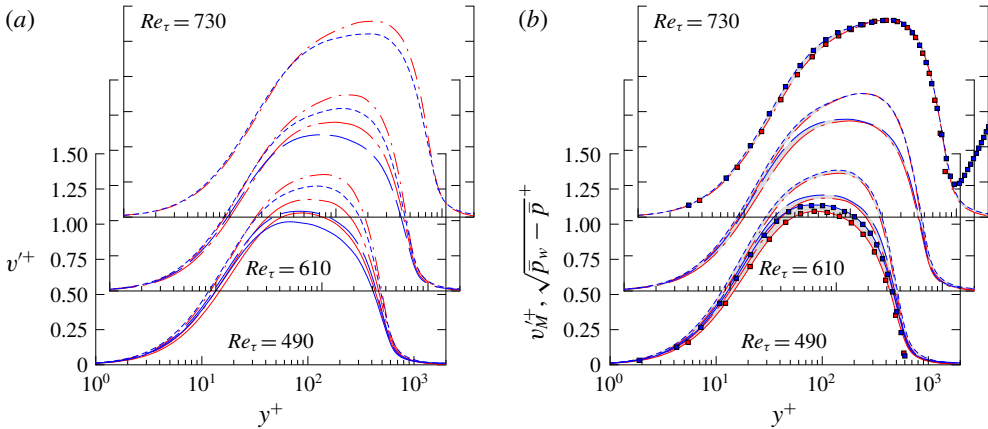
FIGURE 19. (Colour online) Comparison of wall-normal Reynolds fluctuations at $Re_\tau = 490$, 610 and 730 in (*a*) unscaled formulation $v'^+ = \sqrt{\overline{v'^2}}/u_\tau$ and (*b*) density-scaled formulation $v_M'^+ = \sqrt{\overline{\rho}/\overline{\rho}_w}\sqrt{\overline{v'^2}}/u_\tau$ as lines. Filled square symbols in (*b*) represent the pressure distribution $\sqrt{\overline{p}_w - \overline{p}}/(\sqrt{\overline{\rho}_w}u_\tau)$ as already given in figure 18(*a*). Only corresponding cases of comparable β_K-values are given. All red: ——— *iZPG*, ——·· *iAPG*$_{\beta_K=0.19}$, —·— *iAPG*$_{\beta_K=0.58}$. All blue: ——— *cZPG*, ——– *cAPG*$_{\beta_K=0.15}$, ––––– *cAPG*$_{\beta_K=0.55}$.

If the pressure distributions and the corresponding Morkovin-scaled velocity fluctuations are compared in (*b*) first, an almost complete agreement can be established up to the boundary-layer edge $\delta_{99}^+ = Re_\tau$. Thus, both the validity of (4.7) for compressible PG cases with similar β_K-values and the approximate validity of Morkovin's scaling for the wall-normal velocity fluctuations $\overline{v'^2}$ are implied. If assessed against the untransformed distributions in (*a*), no complete scaling success can be found for the ZPG cases. While the incompressible distribution is noticeably above the compressible one in the unscaled representation in (*a*), the incompressible one is noticeably below the compressible one in the density-scaled representation in (*b*), see also Wenzel *et al.* (2018*b*). In contrast, the scaling success is better for the APG cases, mainly caused by the smaller Mach numbers of the APG cases at the given Reynolds numbers.

4.2. *Local mean-flow statistics*

In the previous section both the non-dimensional turbulent stresses $-\overline{\rho u'v'}/\overline{\tau}_w$ and $\overline{\rho v'^2}/\overline{\tau}_w$ have been found to be almost unaffected by compressibility effects for PG cases with comparable β_K-values in the investigated Mach- and Reynolds-number ranges. The so confirmed validity of Morkovin's scaling/hypothesis for the given CPG TBLs further implies the approximate validity of van Driest's transformation in the inner region of the TBL as discussed before. In this section, both the profiles of the local mean-flow velocity $\overline{u}$ and the streamwise velocity fluctuations $\overline{u'^2}$ are investigated in more detail. To this end, all results are discussed separately for the sub- and supersonic regime first in order to work out the effect of varying PGs on the respective regime.

4.2.1. *Mean-flow velocity profiles $\overline{u}$*

The streamwise mean-flow velocity profiles $\overline{u}^+$ are given in figures 20 and 21 for all sub- and supersonic cases, respectively, the inner layer on the left, the outer layer on the right. All results are extracted at the same three Reynolds numbers $Re_\tau = 490$, 610 and 730 if available, except for the supersonic FPG case extracted at $Re_\tau = 360$. All velocity profiles are located in regions of well-developed β_K-parameter distributions, see figure 10.

In the subsonic cases (figure 20) often reported results can be seen. Whereas the velocity profiles are shifted down to lower $\overline{u}^+$-values in the logarithmic region with increasing β_K, they are lifted in the wake region. Evaluated at $y^+ \approx 50$ and $y^+ = \delta_{99}^+ = Re_\tau$, this shift is almost constant for all given Reynolds numbers.

Mainly due to the varying effect of compressibility in the streamwise direction, the supersonic APG results as given in figure 21 are more difficult to interpret. In the logarithmic region, both the opposing effects of compressibility (lifting for decreasing streamwise Mach numbers) and APGs (shifting down for increasing APG strength) balance each other, yielding the almost same distributions in the logarithmic layer for all APG cases in figure 21(*a*) (cf. also figure 12 or 17*a*). In the wake region where both effects constructively overlap (lifting up for increasing APG strength and decreasing streamwise Mach number), $\overline{u}^+$-values are increased with increasing β_K, see $y^+ = Re_\tau = \delta_{99}^+$ in figure 21(*b*). However, due to the decreasing influence of compressibility in the streamwise direction, this shift is not expected to be constant for increasing Reynolds numbers. An assessment of the supersonic FPG case shows inverted trends.

4.2.2. *The van Driest transformation*

Figures 22 and 23 illustrate the untransformed and van Driest transformed mean-flow distributions $\overline{u}^+$ and $\overline{u}_{VD}^+$ (4.2), respectively, both for the subsonic $iAPG_{\beta_K=0.19}$ and $iAPG_{\beta_K=0.58}$ cases and the compressible $cAPG_{\beta_K=0.15}$ and $cAPG_{\beta_K=0.55}$ cases. Based on the total shear-stress distributions $\overline{\tau}_t$ discussed in the previous section, the compressible cases should coincide with the incompressible ones if the van Driest transformation is successful.

For the inner layer, figure 23(*a*), the supersonic velocity profiles $\overline{u}_{VD}^+$ are almost perfectly shifted into their subsonic counterparts, compare figures 22(*a*) and 23(*a*). In the wake region for $y^+ \gtrsim 100$ (figure 23*b*), the subsonic $iAPG_{\beta_K=0.19}$ and supersonic $cAPG_{\beta_K=0.15}$ cases are almost identical, whereas the supersonic $cAPG_{\beta_K=0.55}$ case lies noticeably below the subsonic $iAPG_{\beta_K=0.58}$ case. In the ZPG case, however, the van Driest transformed distributions lie above the incompressible references if compared at the same Re_τ, see Wenzel *et al.* (2018*b*). Consequently, the wake distribution of the van Driest transformed velocity profiles is increasingly underestimated with increasing APG strength. For the weak $cAPG_{\beta_K=0.15}$ case, the underestimating effect by the APG balances the overestimating effect by compressibility, whereas it is overcompensated for the stronger $cAPG_{\beta_K=0.55}$ case. Thus, with increasing Re_τ and thus decreased Mach number in APG flows, also the success of van Driest's transformation varies. In some contrast to the ZPG study however, the van Driest transformation can be denoted to be still approximately valid for the wake region of the present PG cases, since compressibility effects are significantly reduced, although not being completely excluded.
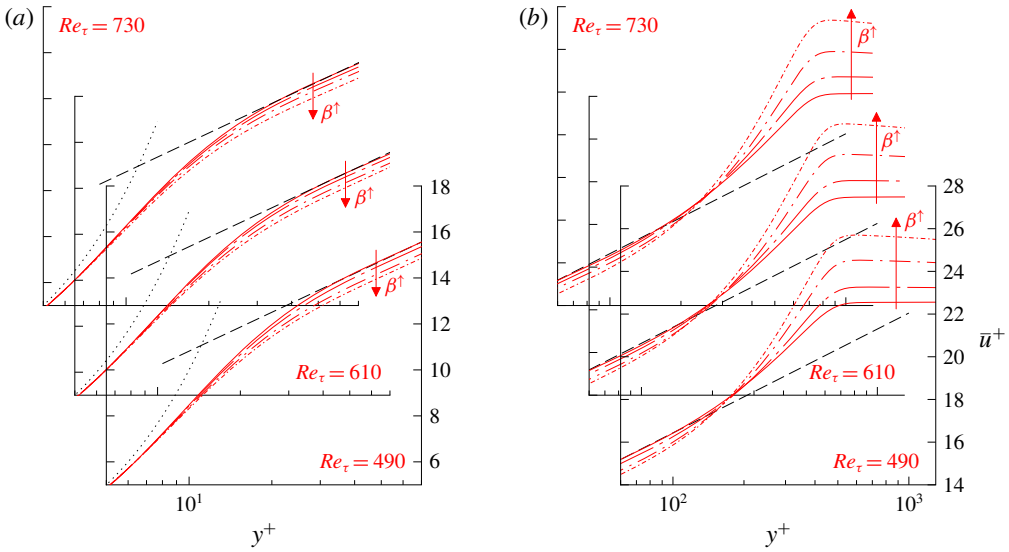
FIGURE 20. (Colour online) Comparison of subsonic mean-flow velocity profiles $\overline{u}^+$ at $Re_\tau = 490$, 610 and 730. Black dotted lines denote the viscous sublayer $\overline{u}^+ = y^+$, dashed black lines the logarithmic region $\overline{u}^+ = 1/k \ln y^+ + C$ with $k = 0.41$ and $C = 5.2$. All red: —— $iZPG$, ——·· $iAPG_{\beta_K=0.19}$, —·— $iAPG_{\beta_K=0.58}$, ——··· $iAPG_{\beta_K=1.05}$.
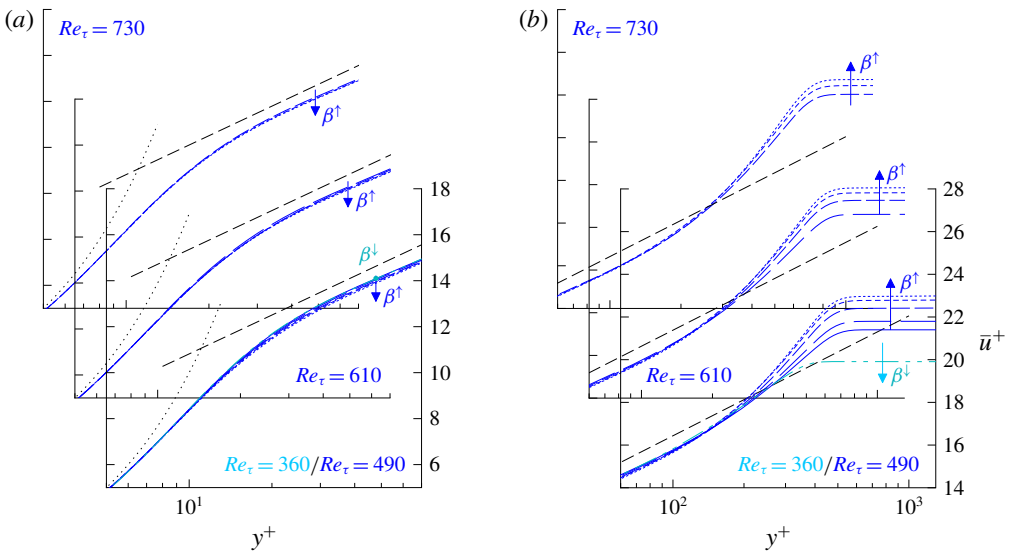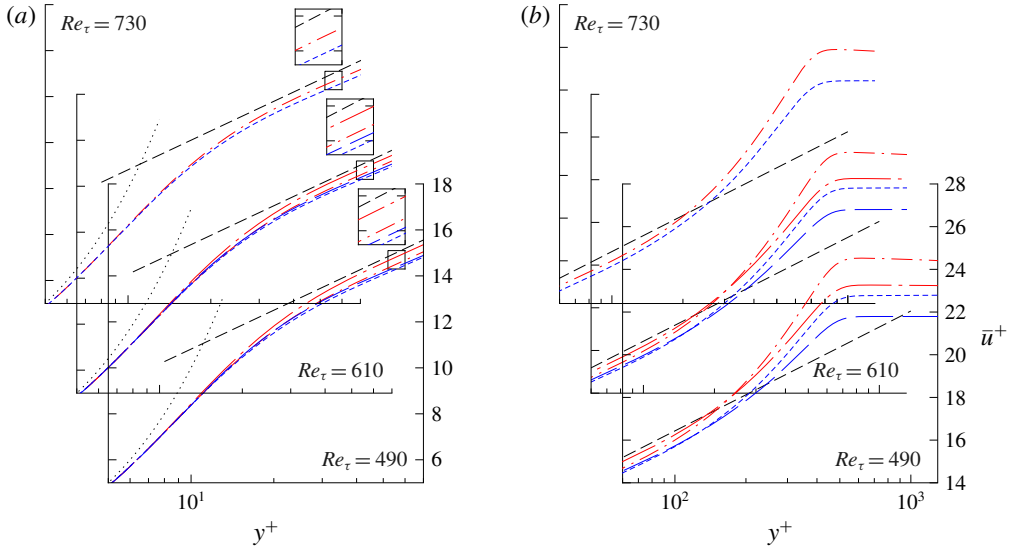

FIGURE 21. (Colour online) Comparison of supersonic mean-flow velocity profiles $\overline{u}^+$ at $Re_\tau = 490$, 610 and 730 for ZPG/APG and $Re_\tau = 360$ for FPG cases. Further information are given in figure 20. All blue: —— $cZPG$, ——– $cAPG_{\beta_K=0.15}$, —·— $cAPG_{\beta_K=0.42}$, ––––– $cAPG_{\beta_K=0.55}$, ······ $cAPG_{\beta_K=0.69}$. Cyan: —·–· $cFPG_{\beta=-0.35}$.

FIGURE 22. (Colour online) Comparison of sub- and supersonic mean-flow velocity profiles $\bar{u}^+$ at $Re_\tau = 490$, 610 and 730. Black dotted lines denote the viscous sublayer $\bar{u}^+ = y^+$, dashed black lines the logarithmic region $\bar{u}^+ = 1/k \ln y^+ + C$ with $k = 0.41$ and $C = 5.2$. Only corresponding cases of comparable β_K-values are given. All red: ———— $iZPG$, ———·· $iAPG_{\beta_K=0.19}$, ——·— $iAPG_{\beta_K=0.58}$. All blue: ———— $cZPG$, ———— $cAPG_{\beta_K=0.15}$, ----- $cAPG_{\beta_K=0.55}$.
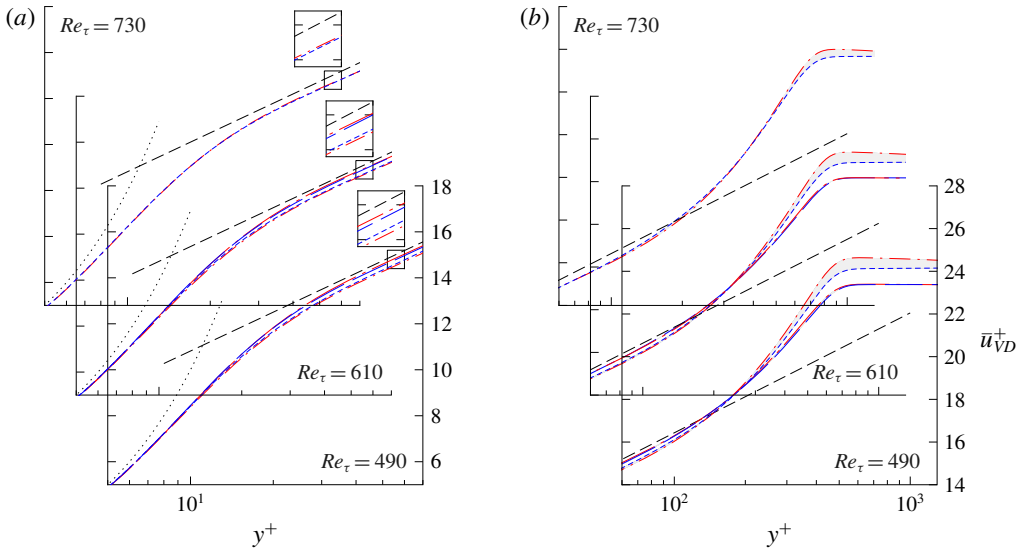
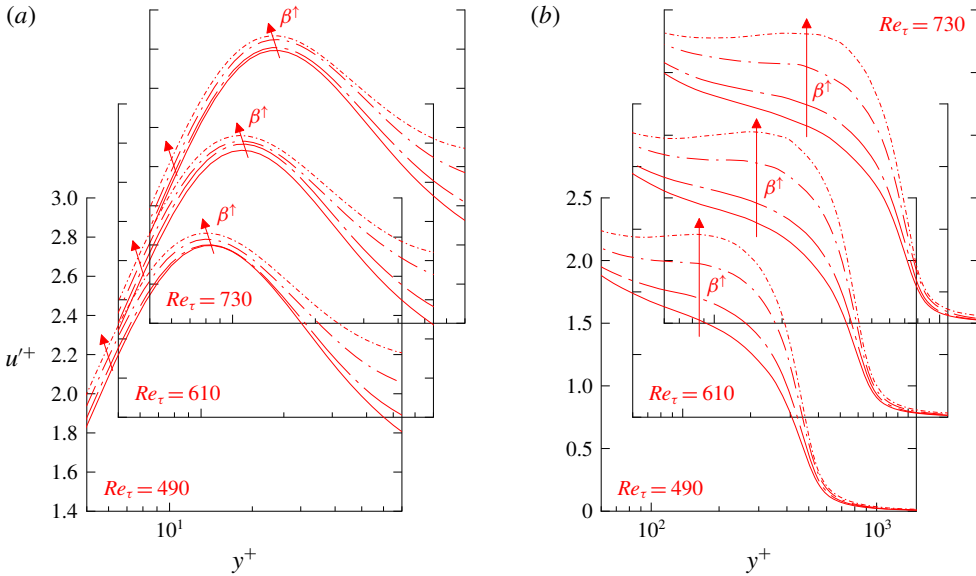FIGURE 23. (Colour online) Same as figure 22, but for van Driest transformed profiles $\bar{u}^+_{VD}$.

FIGURE 24. (Colour online) Comparison of subsonic streamwise Reynolds fluctuations $u'^+ = \sqrt{\overline{u'^2}}/u_\tau$ at $Re_\tau = 490$, 610 and 730. Solid lines represent the ZPG case, non-solid lines APG cases. Arrows denote the direction of increasing APG strength β_K. Red: ——— $iZPG$, ———·· $iAPG_{\beta_K=0.19}$, —·—— $iAPG_{\beta_K=0.58}$, −·−·− $iAPG_{\beta_K=1.05}$.
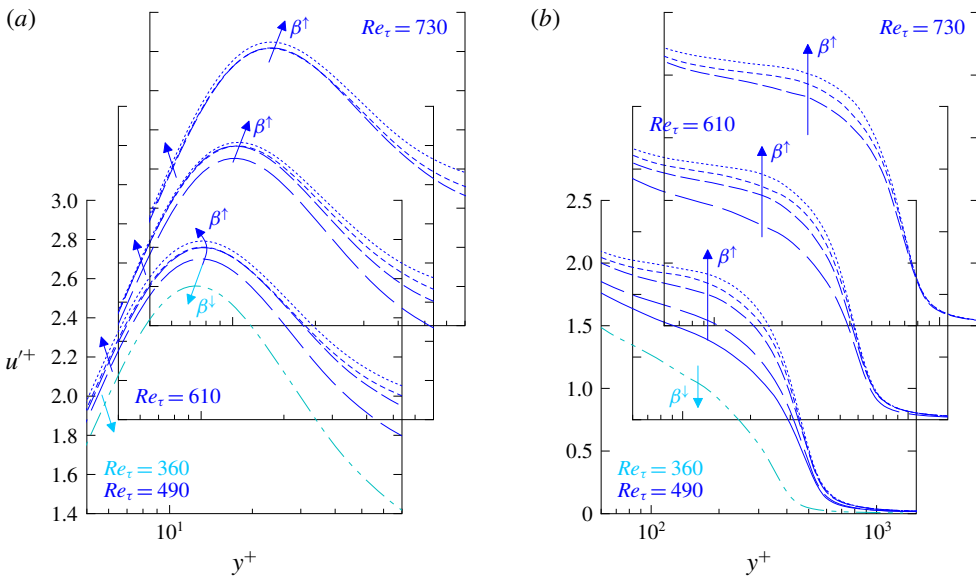

FIGURE 25. (Colour online) Comparison of supersonic streamwise Reynolds fluctuations $u'^+ = \sqrt{\overline{u'^2}}/u_\tau$ at $Re_\tau = 490$, 610 and 730 for ZPG/APG and $Re_\tau = 360$ for FPG cases. Blue: ——— $cZPG$, ———— $cAPG_{\beta_K=0.15}$, ———· $cAPG_{\beta_K=0.42}$, −−−−− $cAPG_{\beta_K=0.55}$, −−−−−− $cAPG_{\beta_K=0.69}$. Cyan: —·−−· $cFPG_{\beta=-0.35}$.
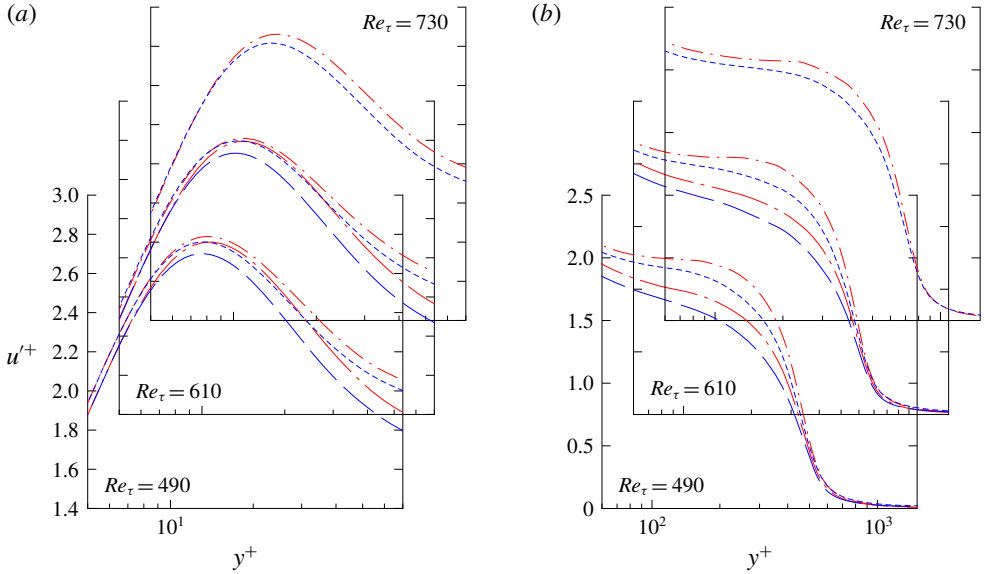
FIGURE 26. (Colour online) Comparison of sub- and supersonic streamwise Reynolds fluctuations $u'^+ = \sqrt{\overline{u'^2}}/u_\tau$ at $Re_\tau = 490$, 610 and 730. Only corresponding cases of comparable β_K-values are given. All red: ——·· $iAPG_{\beta_K=0.19}$, ——·— $iAPG_{\beta_K=0.58}$. All blue: ———– $cAPG_{\beta_K=0.15}$, - - - - - - $cAPG_{\beta_K=0.55}$.
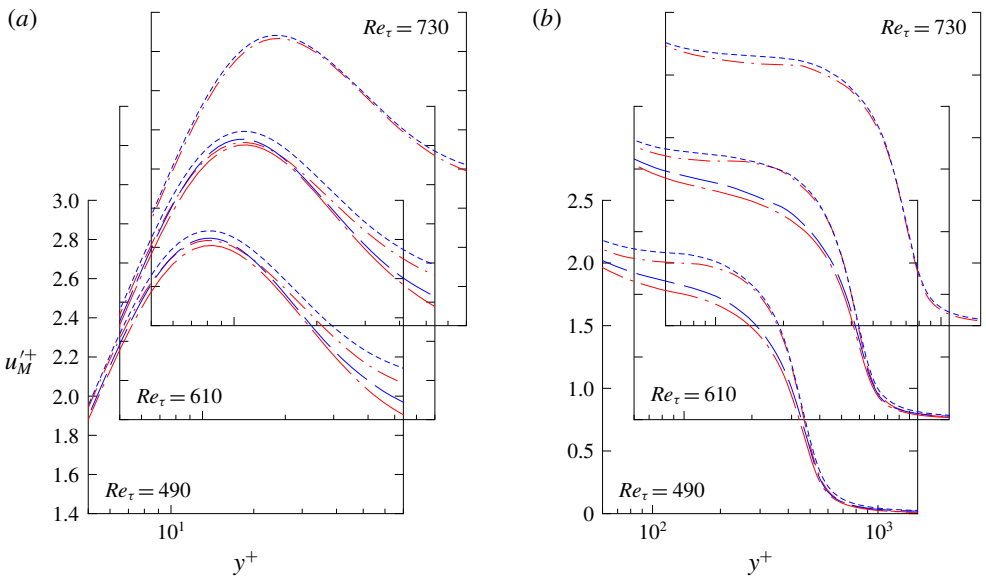

FIGURE 27. (Colour online) Same as figure 26, but for density-scaled streamwise Reynolds fluctuations, $u'^+_M = \sqrt{\overline{\rho}/\overline{\rho}_w}\sqrt{\overline{u'^2}}/u_\tau$.

4.2.3. *Reynolds fluctuations* $\overline{u'^2}$

In the same representation as for the mean velocity profiles, the streamwise Reynolds-averaged velocity fluctuations $u'^+ = \sqrt{\overline{u'^2}}/u_\tau$ are given in figures 24 and 25 separately for the sub- and supersonic cases, respectively.

At first and in extension of figure 16, the inner layer of the Reynolds fluctuations is revisited in figures 24(*a*) and 25(*a*). In comparison to the compressible ZPG cases (Wenzel *et al.* 2018*b*), the Reynolds fluctuation profiles do not match for different PG cases near the wall for $y^+ \lesssim 10$. The distributions are increased for APGs and decreased for FPGs causing higher and lower values for $(\partial u'^+/\partial y^+)|_w$, respectively, see figure 16(*c*). The position of the near-wall fluctuation maximum is increased for APGs and decreased for FPGs as already has been seen in figure 16(*a,b*). However, in combination with the effect of varying Mach number in streamwise direction, the interpretation of the peak's absolute value is again complex for the supersonic cases. Consistently given for both the sub- and supersonic cases in figures 24(*b*) and 25(*b*), the well-known second maximum appears in the outer region of the boundary layer, see Skote *et al.* (1998) and Kitsios *et al.* (2017), for instance.

4.2.4. *Morkovin scaling*

Both in its unscaled $u'^+ = \sqrt{\overline{u'^2}}/u_\tau$ and Morkovin-scaled representation $u_M'^+ = \sqrt{\overline{\rho/\rho_w}}\sqrt{\overline{u'^2}}/u_\tau$, the Reynolds fluctuations are depicted in figures 26 and 27, respectively. As for the mean-flow distributions, only the subsonic $iAPG_{\beta_K=0.19}$ and $iAPG_{\beta_K=0.58}$ cases and the compressible $cAPG_{\beta_K=0.15}$ and $cAPG_{\beta_K=0.55}$ cases are depicted, for which the PG influence is comparable.

If compared in the unscaled representation in figure 26, both the inner and the outer peaks of the supersonic cases are reduced compared to the subsonic results. In the Morkovin-scaled representation in figure 27, both the inner and the outer peaks of the supersonic cases are slightly lifted above the subsonic results. It is noted, however, that this behaviour has been also observed in the ZPG study to a similar extent, see Wenzel *et al.* (2018*b*), and is therefore much more attributed to compressibility than to PG effects. Morkovin's scaling thus also can be confirmed for the present PG cases to a comparable extent as for the ZPG cases, which further implies the Mach-number invariance of the non-dimensionalized streamwise $\overline{\rho u''^2}/\overline{\tau}_w$ stress

$$\frac{\overline{\rho u''^2}}{\overline{\tau}_w}\bigg|_{PG} \approx \frac{\overline{\rho}}{\overline{\rho}_w}\frac{\overline{u'^2}}{u_\tau^2}\bigg|_{PG} = f(PG) \neq f(M). \tag{4.9}$$

5. Conclusions

The main goal of the present study is to identify the effects of pressure gradients as uniquely as possible on compressible flat-plate turbulent boundary layers (TBLs). To this end, spatial DNS of compressible, self-similar PG TBLs have been conducted and analysed both for sub- and supersonic inflow Mach numbers for the first time. The equilibrium character of the investigated flows allows for a direct comparison of sub- and supersonic cases. It turned out that the kinematic Rotta–Clauser parameter β_K built by the incompressible boundary-layer displacement thickness as the length scale is the right similarity parameter, see also Gibis *et al.* (2019). Thus, by regarding both incompressible and compressibility transformed compressible counterparts, the isolated effects of continuous PGs can be evaluated, and the validity of the most common compressibility transformations scrutinized.

One ZPG and three APG cases have been investigated for the subsonic regime (inflow Mach number $M_{\infty,0} = 0.5$, $\beta_K = 0$, 0.19, 0.58, 1.05) and one FPG, one ZPG and four APG cases for the supersonic regime (inflow Mach number $M_{\infty,0} = 2.0$, $\beta_K = -0.18$, 0, 0.15, 0.42, 0.55, 0.69). All cases are characterized by long regions of virtually constant β_K.

The evaluation of the subsonic APG cases is consistent with the known trends gained by incompressible investigations. Whereas the c_f-distributions, for instance, are decreased with increasing APG-strength, the shape-factor values H are increased. If plotted in wall units, local mean-flow profiles of subsonic APG cases are shifted down in the logarithmic layer and lifted in the wake region; the turbulent activity is significantly enhanced through the whole boundary layer, and the streamwise velocity fluctuation profiles show a second peak in the outer layer for increasing APGs.

The interpretation of the supersonic flow field is more complex since two effects are counteracting. While streamtubes are tending to diverge in the subsonic near-wall region in the presence of APGs, they tend to converge in the supersonic part above. The resulting boundary-layer thicknesses δ_{99} as well as the c_f-distribution, for instance, are therefore in a comparable range for all PG cases. In accordance with Spina *et al.* (1994), the switch-over value of $M_e \approx 1.8$ can be confirmed, below which supersonic PG TBLs are increasingly dominated by the subsonic part of the boundary layer. If plotted in wall units and compared to the ZPG case, local mean-flow profiles of supersonic cases are only slightly influenced in the logarithmic layer due to the counteracting effect of PGs and compressibility. In the wake region where both effects superpose constructively, profiles are lifted for APGs and shifted down for FPGs cases. The turbulent fluctuations are influenced in an almost identical manner as for the subsonic cases.

For both sub- and supersonic cases the recovery factor is noticeably influenced by PGs, i.e. decreased for APG and increased for FPG cases, but stays almost constant in its spatial evolution for equilibrium cases.

A comparison of the total shear-stress distributions $\overline{\tau}_t/\overline{\tau}_w$ yields almost identical profiles for sub- and supersonic cases if evaluated at same β_K- and Re_τ-values, although there is no constant stress layer near the wall anymore. An APG increases $\overline{\tau}_t/\overline{\tau}_w$ for $y^+ \gtrsim 2$ due to increased turbulent activity, an FPG does the opposite. Since Mach-number and PG influences on the local mean shear-stress distributions $\overline{\mu}\,\partial\overline{u}/\partial y/\overline{\tau}_w$ are virtually negligible, also the turbulent shear-stress distributions $-\overline{\rho u'v'}/\overline{\tau}_w$ are similar to each other for similar β_K-cases. The same holds for the turbulent stresses in the wall-normal direction $\overline{\rho v'^2}/\overline{\tau}_w$, which thus implies the Mach-number invariance of PG effects in the compressible regime and thus the approximate validity of Morkovin's scaling for compressible PG TBLs at least in the near equilibrium case. The Morkovin-scaled $\overline{u'^2}$ fluctuations can reproduce the respective incompressible distributions for comparable β_K values with uncertainties being approximately in the same range as for ZPG cases. It is pointed out, however, that the assumption of a constant total stress region near the wall – as sometimes assumed in the scaling's derivation – is not a necessary condition. Morkovin's hypothesis that 'the essential dynamics of supersonic shear flows will follow the incompressible patter' thus still holds for TBLs subjected to PGs.

Implied by both the validity of Morkovin's scaling and the two-dimensional turbulent y-momentum boundary-layer equation, also the mean pressure distributions

$(\overline{p}_{w \approx e} - \overline{p})/\overline{\tau}_w$ and thus also the pressure fluctuations $\sqrt{\overline{p'^2}}/\overline{\tau}_w$ are found to compare for different Mach-number cases for same β_K-values.

Concerning the van Driest transformation, the logarithmic layer of compressible PG cases can be reliably transformed into the respective nearly incompressible counterparts. The velocity in the wake region of the van Driest transformed profiles is increasingly underestimated with increasing APG strength and thus depends on the particular PG distribution. Since the wake region is also influenced by compressibility effects varying in the streamwise direction if evaluated at same Re_τ, uncertainties of the van Driest transformation are not readily predictable for complex PG flows. Nevertheless, the van Driest transformation still reduces compressibility effects significantly.

Acknowledgements

Appendix A. Grid convergence analysis

The grid convergence analysis is performed for the most restricting subsonic *iZPG* case and the supersonic $cAPG_{\beta_K=0.69}$ case, see table 3(b). For the subsonic case where low Reynolds numbers are most restricting, the domain size for the analysis is reduced to $(L_x \times L_y \times L_z)/\delta_{99,0} = 170 \times 34 \times 4\pi$. This corresponds to half the length and one third the width of the domain size used in the study, see table 3(a). For the supersonic case, the analysis is performed on the domain size used in the study with $(L_x \times L_y \times L_z)/\delta_{99,0} = 500 \times 34 \times 12\pi$ to allow an evaluation at the most restricting high Reynolds numbers. The grid resolution is varied using 70 %, 100 % and 130 %, respectively, in the three directions for the subsonic cases, and 40 %, 60 %, 80 % and 100 % for the supersonic case, see table 4. The resulting grid resolution is summarized in table 4 in terms of wall units next to the resulting skin-friction coefficients c_f and the shape-factor values H. Subsonic case results are evaluated at $Re_\tau = 480$ (averaging time $\Delta t u_e/\delta_{99} \approx 850$), supersonic case results at $Re_\tau = 700$ (averaging time about $\Delta t u_e/\delta_{99} \approx 580$).

Given in figure 28(*a*), cf. figure 17, the grid resolution is assessed by a comparison of the mean shear-stress distributions $\overline{\mu}(\partial \overline{u}/\partial y)/\overline{\tau}_w$ and turbulent shear-stress distributions $-\overline{\rho u'' v''}/\overline{\tau}_w$. According to figure 16(*a*) and figures 24(*b*) or 25(*b*), both the peak values u'^+_{max} and the wall-normal distributions in the outer layer of the turbulent velocity fluctuations $u'^+ = \sqrt{\overline{u'^2}}/u_\tau$ are given in figure 28(*b,c*), respectively. Both values have been found to be the most sensitive ones to a poor grid resolution. As illustrated, both the results of the subsonic *iZPG*_100 % and *iZPG*_130 % cases, and of the supersonic $cAPG_{\beta_K=0.69}$_80 % and $cAPG_{\beta_K=0.69}$_100 % cases, are in good agreement. All given results can therefore be regarded as grid converged.
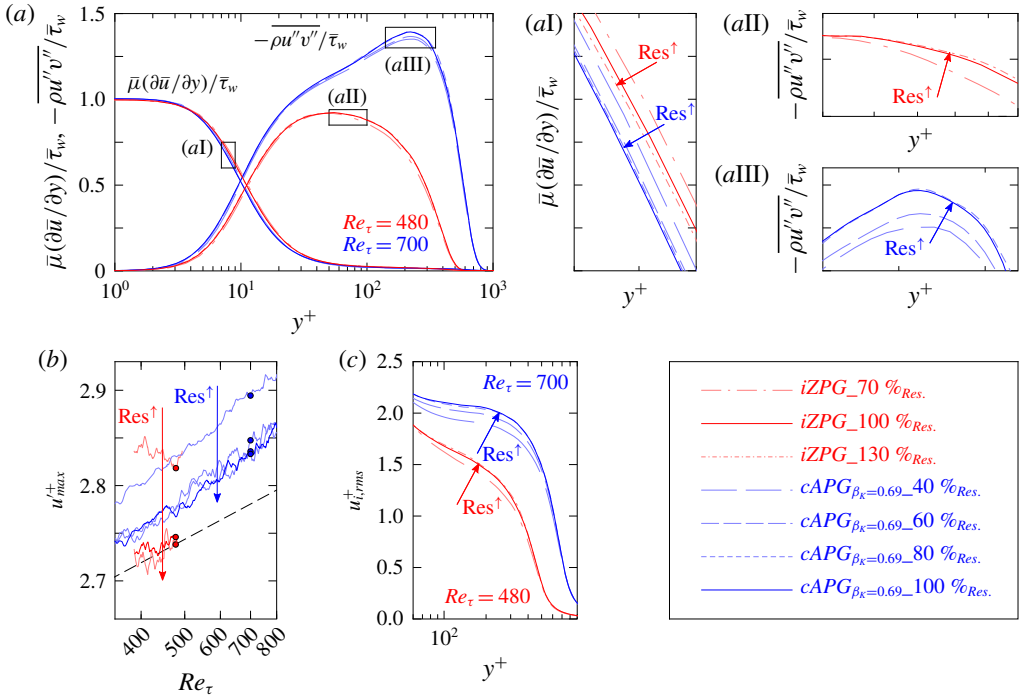
FIGURE 28. (Colour online) Grid resolution analysis for the subsonic *iZPG* case ($Re_\tau = 480$) and supersonic $cAPG_{\beta_K} = 0.69$ case ($Re_\tau = 700$). (*a*) Mean shear-stress distributions $\overline{\mu(\partial\overline{u}/\partial y)}/\overline{\tau}_w$ and turbulent shear-stress distributions $-\overline{\rho u'' v''}/\overline{\tau}_w$, (*b*) wall-near peak value u^{+}_{max} and (*c*) wall-normal distribution in the outer layer of the streamwise velocity fluctuation $u'^{+} = \sqrt{\overline{u'^2}}/u_\tau$.

		nx	ny	nz	Δx^+	Δy^+_w	Δz^+	$c_f \times 10^3$	H
$Re_\tau = 480$:	$iZPG\_70\%$	875	200	196	24.2	0.85	7.9	3.834	1.532
	$iZPG\_100\%$	1250	270	280	16.8	0.70	5.5	3.792	1.553
	$iZPG\_130\%$	1625	328	360	12.9	0.63	4.3	3.793	1.555
$Re_\tau = 700$:	$cAPG_{\beta_K=0.69}\_40\%$	2000	120	384	22.8	0.75	9.0	2.588	2.399
	$cAPG_{\beta_K=0.69}\_60\%$	3000	180	576	15.1	0.62	5.8	2.507	2.416
	$cAPG_{\beta_K=0.69}\_80\%$	4000	240	768	11.3	0.47	4.4	2.459	2.418
	$cAPG_{\beta_K=0.69}\_100\%$	5000	300	960	9.00	0.40	3.5	2.452	2.419

TABLE 4. Grid resolution analysis for the subsonic *iZPG* case ($Re_\tau = 480$) and supersonic $cAPG_{\beta_K} = 0.69$ case ($Re_\tau = 700$). Given parameters are the number of numerical grid points *nx*, *ny* and *nz* as well as the resulting grid resolutions Δx^+, Δy^+_w and Δz^+ in the streamwise, wall-normal and spanwise directions, respectively. Additionally given are the skin-friction coefficient c_f and the shape factor H_{12}.

Appendix B. Vortex visualization

Figures 29 and 30 depict iso-levels of the λ_2-criterion computed from the non-dimensionalized flow field $u_i = u_i/u_{\infty,0}$ with $\lambda_2 = -0.05\, u_e(x)/u_{\infty,0}$ for sub-
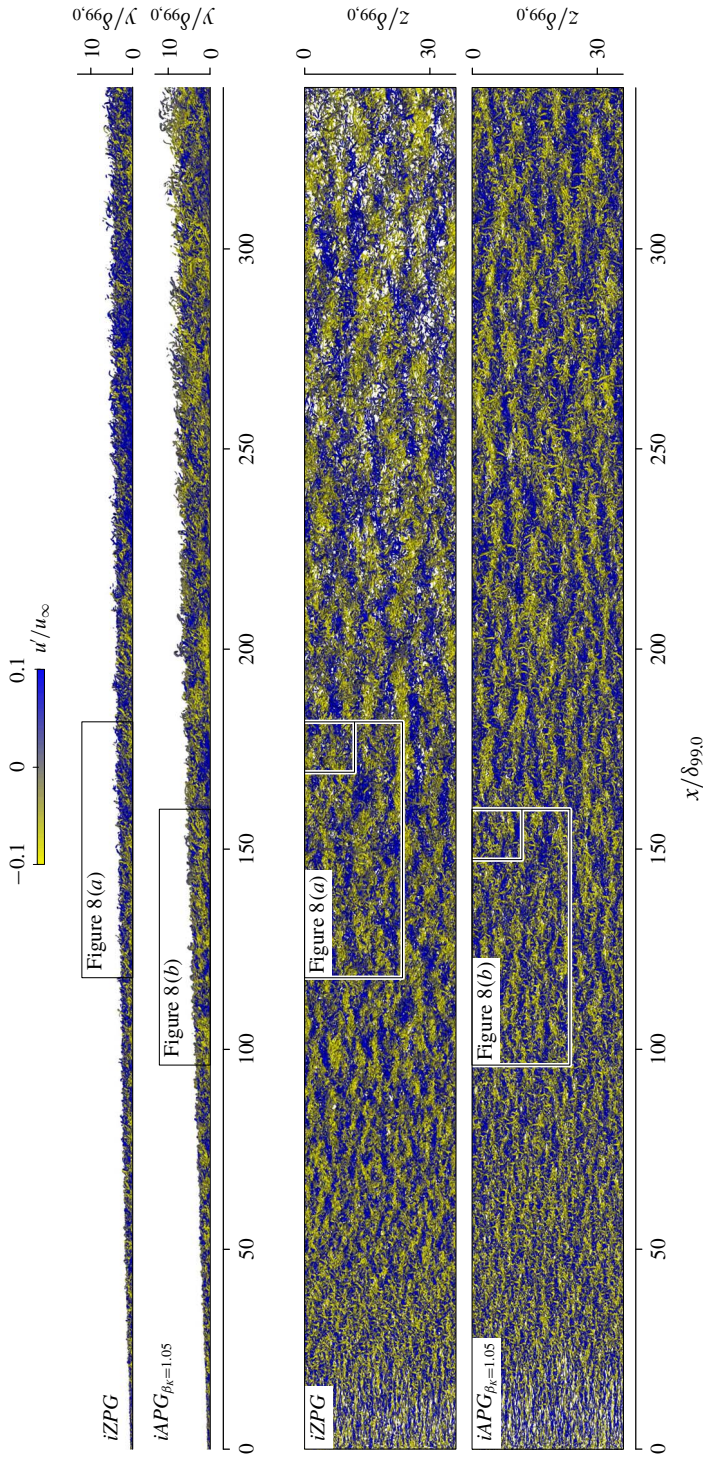
FIGURE 29. (Colour online) Snapshots of vortices by iso-surfaces of the λ_2-criterion with $\lambda_2 = -0.05u_e(x)/u_{\infty,0}$ for the subsonic *iZPG* case and the strongest subsonic *iAPG*$_{\beta_K=1.05}$ case. Colour depicts the fluctuation amplitude of the streamwise velocity component $u'/u_{\infty,0}$. The complete main region of the simulation domain is shown, the bordered regions are depicted in detail in figure 8.
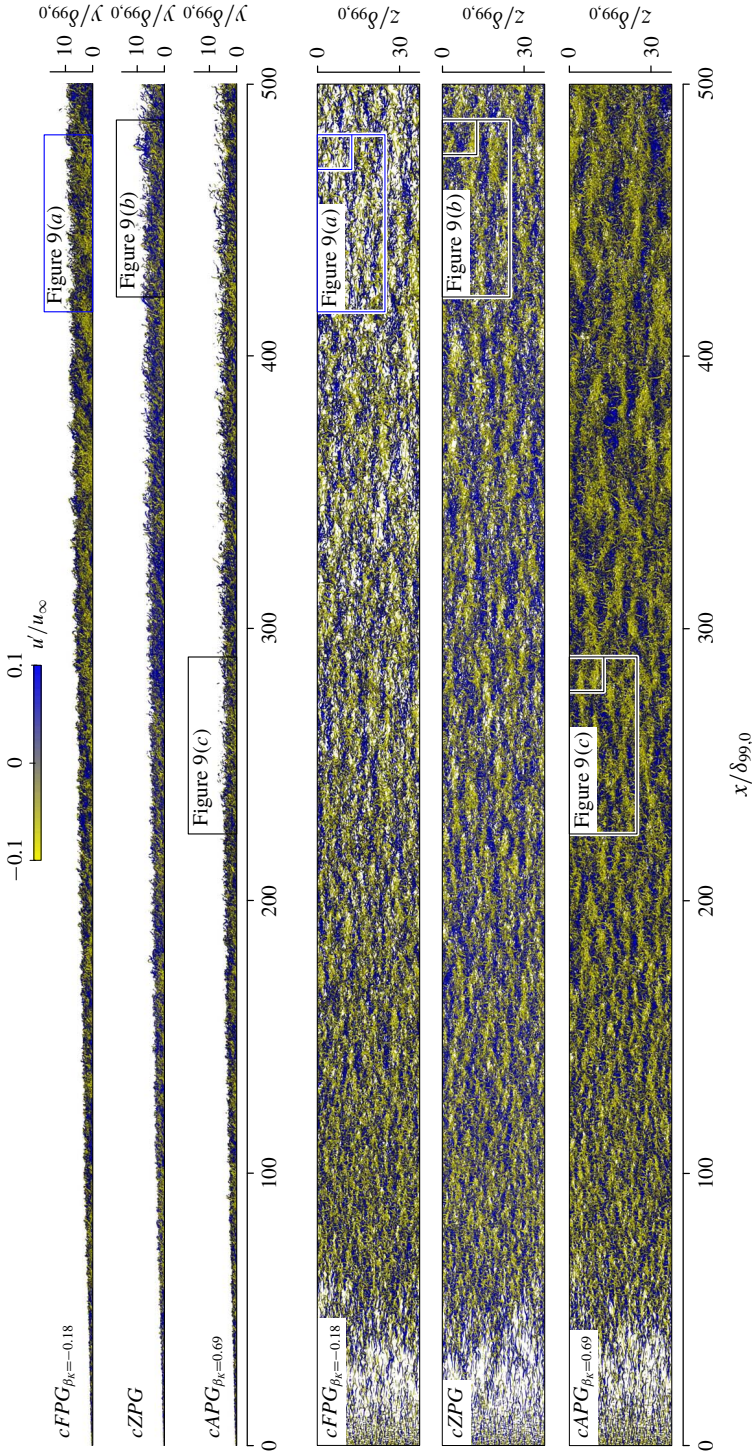
FIGURE 30. (Colour online) Snapshots of vortices by iso-surfaces of the λ_2-criterion with $\lambda_2 = -0.05 u_e(x)/u_{\infty,0}$ for the supersonic $cFPG_{\beta_K=-0.18}$ case, the supersonic $cZPG$ case and the strongest supersonic $cAPG_{\beta_K=0.69}$ case. Colour depicts the fluctuation amplitude of the streamwise velocity component $u'/u_{\infty,0}$. The complete main region of the simulation domain is shown, the bordered regions are depicted in detail in figure 9.

and supersonic cases. The complete main region of the simulation domain is shown, the bordered regions are located at $Re_\tau = 490$ (FPG at $Re_\tau = 360$) and are illustrated in detail in figures 8 and 9.

REFERENCES

ADAMS, N. A. 2000 Direct simulation of the turbulent boundary layer along a compression ramp at $M = 3$ and $Re_\theta = 1685$. *J. Fluid Mech.* **420**, 47–83.

ARDONCEAU, P. L. 1984 The structure of turbulence in a supersonic shock-wave/boundary-layer interaction. *AIAA J.* **22** (9), 1254–1262.

ARNETTE, S. A., SAMIMY, M. & ELLIOTT, G. S. 1998 The effects of expansion on the turbulence structure of compressible boundary layers. *J. Fluid Mech.* **367**, 67–105.

BABUCKE, A. 2009 Direct numerical simulation of noise-generation mechanisms in the mixing layer of a jet. PhD thesis, University of Stuttgart.

BOBKE, A., VINUESA, R., ÖRLÜ, R. & SCHLATTER, P. 2017 History effects and near equilibrium in adverse-pressure-gradient turbulent boundary layers. *J. Fluid Mech.* **820**, 667–692.

BOWERSOX, R. D. W. & BUTER, T. A. 1996 Turbulence measurements in a Mach 2.9 boundary layer including mild pressure gradients. *AIAA J.* **34** (12), 2479–2483.

BRADSHAW, P. 1973 Effects of streamline curvature on turbulent flow. *Tech. Rep.* Advisory Group for Aerospace Research and Development Paris.

BRADSHAW, P. 1974 The effect of mean compression or dilatation on the turbulence structure of supersonic boundary layers. *J. Fluid Mech.* **63**, 449–464.

CEBECI, T. & BRADSHAW, P. 1984 *Physical and Computational Aspects of Convective Heat Transfer*. Springer Science & Business Media.

CHAUHAN, K. A., MONKEWITZ, P. A. & NAGIB, H. M. 2009 Criteria for assessing experiments in zero pressure gradient boundary layers. *Fluid Dyn. Res.* **41** (2), 21404.

DONOVAN, J. F., SPINA, E. F. & SMITS, A. J. 1994 The structure of a supersonic turbulent boundary layer subjected to concave surface curvature. *J. Fluid Mech.* **259**, 1–24.

DÖRR, P. C. 2018 Numerical investigations of crossflow transition control using plasma actuators. PhD thesis, University of Stuttgart.

DUSSAUGE, J. P. & GAVIGLIO, J. 1987 The rapid expansion of a supersonic turbulent flow: role of bulk dilatation. *J. Fluid Mech.* **174**, 81–112.

FANG, J., YAO, Y., ZHELTOVODOV, A. A., LI, Z. & LU, L. 2015 Direct numerical simulation of supersonic turbulent flows around a tandem expansion-compression corner. *Phys. Fluids* **27** (12), 125104.

FERNANDO, E. M. & SMITS, A. J. 1990 A supersonic turbulent boundary layer in an adverse pressure gradient. *J. Fluid Mech.* **211**, 285–307.

FERNHOLZ, H.-H., DUSSAUGE, J. P., FINLAY, P. J., SMITS, A. J. & RESHOTKO, E. 1989 A survey of measurements and measuring techniques in rapidly distorted compressible turbulent boundary layers *Tech. Rep.* Advisory Group for Aerospace Research and Development Neuilly-Sur-Seine.

FERNHOLZ, H.-H., FINLEY, P. J. & MIKULLA, V. 1981 A further compilation of compressible boundary layer data with a survey of turbulence data *Tech. Rep.* Advisory Group for Aerospace Research and Development Neuilly-Sur-Seine.

FRANKO, K. J. & LELE, S. 2014 Effect of adverse pressure gradient on high speed boundary layer transition. *Phys. Fluids* **26** (2), 24106.

GIBIS, T. 2018 Similarity analysis of compressible turbulent equilibrium bboundary-layer with pressure gradients. Master's thesis, University of Stuttgart.

GIBIS, T., WENZEL, C., KLOKER, M. & RIST, U. 2019 Self-similar compressible turbulent boundary layers with pressure gradients. Part 2. Self-similarity analysis of the outer layer. *J. Fluid Mech.* **880**, 284–325.

GUARINI, S. E., MOSER, R. D., SHARIFF, K. & WRAY, A. 2000 Direct numerical simulation of a supersonic turbulent boundary layer at Mach 2.5. *J. Fluid Mech.* **414**, 1–33.

JAYARAM, M., TAYLOR, M. W. & SMITS, A. J. 1987 The response of a compressible turbulent boundary layer to short regions of concave surface curvature. *J. Fluid Mech.* **175**, 343–362.

KELLER, M. A. 2016 Numerical Investigation of Gaseous Film and Effusion Cooling in Supersonic Boundary-Layer-Flows. PhD thesis, University of Stuttgart.

KELLER, M. A. & KLOKER, M. J. 2013 DNS of effusion cooling in a supersonic boundary-layer flow: influence of turbulence. In *44th AIAA Thermophysics Conference*, p. 2897.

KELLER, M. A. & KLOKER, M. J. 2014 Effusion cooling and flow tripping in laminar supersonic boundary-layer flow. *AIAA J.* **53** (4), 902–919.

KELLER, M. A. & KLOKER, M. J. 2016 Direct numerical simulation of foreign-gas film cooling in supersonic boundary-layer flow. *AIAA J.* **55** (1), 99–111.

KITSIOS, V., ATKINSON, C., SILLERO, J. A., BORRELL, G., GUNGOR, A. G., JIMÉNEZ, J. & SORIA, J. 2016 Direct numerical simulation of a self-similar adverse pressure gradient turbulent boundary layer. *Intl J. Heat Fluid Flow* **61**, 129–136.

KITSIOS, V., SEKIMOTO, A., ATKINSON, C., SILLERO, J. A., BORRELL, G., GUNGOR, A. G., JIMÉNEZ, J. & SORIA, J. 2017 Direct numerical simulation of a self-similar adverse pressure gradient turbulent boundary layer at the verge of separation. *J. Fluid Mech.* **829**, 392–419.

KLOKER, M. J. 1997 A robust high-resolution split-type compact FD scheme for spatial direct numerical simulation of boundary-layer transition. *Appl. Sci. Res.* **59** (4), 353–377.

KURZ, H. B. E. & KLOKER, M. J. 2014 Receptivity of a swept-wing boundary layer to micron-sized discrete roughness elements. *J. Fluid Mech.* **755**, 62–82.

LEE, J. H. 2017 Large-scale motions in turbulent boundary layers subjected to adverse pressure gradients. *J. Fluid Mech.* **810**, 323–361.

LEE, J.-H. & SUNG, H. J. 2008 Effects of an adverse pressure gradient on a turbulent boundary layer. *Intl J. Heat Fluid Flow* **29** (3), 568–578.

LINN, J. & KLOKER, M. J. 2008 Numerical investigations of film cooling. In *RESPACE - Key Technologies for Resuable Space Systems* (ed. A. Gülhan), NNFM, vol. 98, pp. 151–169.

LINN, J. & KLOKER, M. J. 2011 Effects of wall-temperature conditions on effusion cooling in a supersonic boundary layer. *AIAA J.* **49** (2), 299–307.

LUKER, J. J., BOWERSOX, W., RODNEY, D. & BUTER, T. A. 2000 Influence of curvature-driven favorable pressure gradient on supersonic turbulent boundary layer. *AIAA J.* **38** (8), 1351–1359.

MORKOVIN, M. V. 1961 Effects of compressibility on turbulent flows. In *Mécanique de la Turbulence* (ed. A. Favre), pp. 367–380. CNRS.

PERRY, A. E., MARUSIC, I. & JONES, M. B. 2002 On the streamwise evolution of turbulent boundary layers in arbitrary pressure gradients. *J. Fluid Mech.* **461**, 61–91.

PIROZZOLI, S. & BERNARDINI, M. 2011 Turbulence in supersonic boundary layers at moderate Reynolds number. *J. Fluid Mech.* **688**, 120–168.

POINSOT, T. J. & LELE, S. K. 1991 Boundary conditions for direct simulations of compressible viscous flows. *J. Comput. Phys.* **101** (1), 104–129.

SCHLATTER, P. & ÖRLÜ, R. 2010 Assessment of direct numerical simulation data of turbulent boundary layers. *J. Fluid Mech.* **659**, 116–126.

SCHMIDT, O. T. 2014 Numerical investigations of instability and transition in streamwise corner-flows. PhD thesis, University of Stuttgart.

SELIG, M. S., ANDREOPOULOS, J., MUCK, K. C., DUSSAUGE, J. P. & SMITS, A. J. 1989 Turbulence structure in a shock wave/turbulent boundary-layer interaction. *AIAA J.* **27** (7), 862–869.

SKÅRE, P. E. & KROGSTAD, P. 1994 A turbulent equilibrium boundary layer near separation. *J. Fluid Mech.* **272**, 319–348.

SKOTE, M., HENNINGSON, D. S. & HENKES, R. A. W. M. 1998 Direct numerical simulation of self-similar turbulent boundary layers in adverse pressure gradients. *Flow Turbul. Combust.* **60**, 47–85.

SMITH, D. R. & SMITS, A. J. 1997 The effects of successive distortions on a turbulent boundary layer in a supersonic flow. *J. Fluid Mech.* **351**, 253–288.

SMITS, A. J. & DUSSAUGE, J.-P. 2006 *Turbulent Shear Layers in Supersonic Flow*. Springer Science & Business Media.

SMITS, A. J. & MUCK, K.-C. 1987 Experimental study of three shock wave/turbulent boundary layer interactions. *J. Fluid Mech.* **182**, 291–314.

SPINA, E. F., SMITS, A. J. & ROBINSON, S. K. 1994 The physics of supersonic turbulent boundary layers. *Annu. Rev. Fluid Mech.* **26** (1), 287–319.

STRATFORD, B. S. 1959 An experimental flow with zero skin friction throughout its region of pressure rise. *J. Fluid Mech.* **5**, 17–35.

SUN, M.-B., HU, Z. & SANDHAM, N. D. 2017 Recovery of a supersonic turbulent boundary layer after an expansion corner. *Phys. Fluids* **29** (7), 76103.

TICHENOR, N. R., HUMBLE, R. A. & BOWERSOX, R. D. W. 2013 Response of a hypersonic turbulent boundary layer to favourable pressure gradients. *J. Fluid Mech.* **722**, 187–213.

TOWNSEND, A. A. 1956 *The Structure of Turbulent Shear Flow*. Cambridge University Press.

VINUESA, R., HOSSEINI, S. M., HANIFI, A., HENNINGSON, D. S. & SCHLATTER, P. 2017 Pressure-gradient turbulent boundary layers developing around a wing section. *Flow Turbul. Combust.* **99** (3–4), 613–641.

WANG, Q.-C., WANG, Z.-G. & ZHAO, Y.-X. 2016a An experimental investigation of the supersonic turbulent boundary layer subjected to concave curvature. *Phys. Fluids* **28** (9), 96104.

WANG, Q.-C., WANG, Z.-G. & ZHAO, Y.-X. 2016b On the impact of adverse pressure gradient on the supersonic turbulent boundary layer. *Phys. Fluids* **28** (11), 116101.

WANG, Q.-C., WANG, Z.-G. & ZHAO, Y.-X. 2017 The impact of streamwise convex curvature on the supersonic turbulent boundary layer. *Phys. Fluids* **29** (11), 116106.

WENZEL, C. 2019 DNS of compressible turbulent boundary layers: pressure-gradient influence and self-similarity. PhD thesis, University of Stuttgart.

WENZEL, C., PETER, J. M. F., SELENT, B., WEINSCHENK, M., RIST, U. & KLOKER, M. J. 2018a DNS of compressible turbulent boundary layers with adverse pressure gradients. In *High Performance Computing in Science and Engineering 2018* (ed. W. E. Nagel), Springer.

WENZEL, C., SELENT, B., KLOKER, M. J. & RIST, U. 2018b DNS of compressible turbulent boundary layers and assessment of data/scaling-law quality. *J. Fluid Mech.* **842**, 428–468.

WHITE, F. M. 2006 *Viscous Fluid Flow*, 3rd edn. McGraw-Hill.

WU, M. & MARTIN, M. P. 2007 Direct numerical simulation of supersonic turbulent boundary layer over a compression ramp. *AIAA J.* **45** (4), 879–889.